



Enhancement of tetracycline photocatalytic degradation under visible light: Unleashing the synergy of Z-scheme Ag₃PO₄/GCN/FeNi-BTC photocatalyst with carbon quantum dots



Manh B. Nguyen ^{a,b,*}, Huan V. Doan ^c, Doan Le Hoang Tan ^{d,e}, Tran Dai Lam ^f

^a Institute of Chemistry, Vietnam Academy of Science and Technology, 18 Hoang Quoc Viet Street, Cau Giay, Hanoi, Viet Nam

^b Graduate University of Science and Technology (GUST), Vietnam Academy of Science and Technology, 18 Hoang Quoc Viet Street, Cau Giay, Hanoi, Viet Nam

^c Research School of Chemistry, The Australian National University, Canberra, ACT 2601, Australia

^d Center for Innovative Materials and Architectures, Ho Chi Minh City, Viet Nam

^e Vietnam National University-Ho Chi Minh City, Ho Chi Minh City, Viet Nam

^f Institute for Tropical Technology (ITT), Vietnam Academy of Science and Technology, 18 Hoang Quoc Viet, Cau Giay, Hanoi, Viet Nam

ARTICLE INFO

Keywords:

Tetracycline degradation
Z-scheme photocatalyst
Carbon quantum dot
MOF
FeNi-BTC
g-C₃N₄

ABSTRACT

This study presents a novel photocatalytic composite, Ag₃PO₄/GCN/FeNi-BTC/CQD (AGF-CQD), synthesized via a green microwave-assisted hydrothermal method, integrating carbon quantum dots (CQDs) derived from aquaculture by-products. The AGF-CQD composite demonstrates superior photocatalytic activity, attributed to enhanced visible light absorption, efficient charge transfer, and improved electron-hole separation. Analytical techniques such as photoluminescence (PL), UV-Vis diffuse reflectance spectroscopy (DRS), and transmission electron microscopy (TEM) validate the composite's structural and optical properties. In tetracycline degradation tests, AGF-CQD outperforms Ag₃PO₄, GCN, FeNi-BTC, and 20 % AGF samples by 5.5, 3.6, 4.4, and 2.3 times, respectively, achieving a remarkable 98.4 % removal rate after 60 min under visible light. Factors affecting degradation, including dosage, concentration, pH, and water source, are investigated. Furthermore, an operating mechanism based on electrochemical properties and the involvement of radicals is proposed. This research offers a sustainable approach to synthesizing efficient photocatalysts for environmental remediation.

Introduction

Antibiotics, essential in treating diseases for both humans and animals, have become pervasive in various environmental sources, including pond water, urban water, groundwater, seawater, and even food [1]. A staggering 50–90 % of administered antibiotics eventually find their way into the environment, contributing to a concerning rise in antibiotic resistance-related deaths, projected by the World Health Organization (WHO) to reach 10 million within the next 35 years [3]. To address this urgent threat, a plethora of technologies have been developed, including filtration, adsorption, photocatalysis, and biodegradation [2–4], with photocatalysis particularly standing out for its eco-friendliness, energy efficiency, and efficacy [5–7].

Within the realm of photocatalysis, graphitic carbon nitride (g-C₃N₄ or GCN) presents itself as a promising option. This non-metallic semiconductor boasts chemical stability, affordability, and the ability to

absorb visible light [8], yet its bulk structure, limited surface area, rapid electron-hole recombination, and subpar charge transfer hamper its photocatalytic efficiency [9]. To address these shortcomings, researchers have explored hybridizing g-C₃N₄ with other porous materials such as metal-organic frameworks (MOFs) and carbon nanotubes (CNTs).

Recently, researchers have developed various photocatalysts based on MOFs. For instance, Xie et al. [10] demonstrated the potent photocatalytic activity of Ag₃PO₄/MIL-53(Fe) in removing antibiotics under visible light irradiation. Similarly, Xu et al. [11] reported that Ag₃PO₄/MIL-100(Fe) photocatalyst decomposed tetracycline 6.8 times faster than MIL-100(Fe). Expanding on the advancements in MOFs for photocatalytic applications, FeNi-BTC emerges as a promising candidate. This bimetallic metal-organic framework (BMOF) forms a robust two-dimensional structure composed of Fe and Ni metal ion clusters linked by H₃BTC linker (trimesic acid), offering a stable architecture and an

* Corresponding author at: Institute of Chemistry, Vietnam Academy of Science and Technology, 18 Hoang Quoc Viet Street, Cau Giay, Hanoi, Viet Nam.
E-mail address: nguyenbamanh@ich.vast.vn (M.B. Nguyen).

impressive surface area surpassing 1000 m²/g [12]. Despite its potential, challenges persist due to the loose integration between semiconductors and MOFs, resulting in low stability and slow electron transfer rates. To overcome these limitations, recent advancements have integrated carbon quantum dots (CQDs) to unleash the synergy of the Z-scheme in heterogeneous photocatalysts. Abundant in functional groups on their surface, CQDs enhance interaction and cohesion with semiconductor materials [13], thus aiding in amalgamating semiconductor components to forge tightly bound composite materials [14]. Consequently, CQDs augment the diffusion, transport, and mobility of charges and vacancies within photocatalytic matrices, resulting in increased photocatalytic efficacy [15]. The synergistic combination of CQDs with g-C₃N₄ has yielded significant improvements, enhancing the electron/hole separation process and elevating the photoelectric current of the CQD/g-C₃N₄ nanocomposite [16]. Combining CQDs with g-C₃N₄, as demonstrated by Li et al. [17], has proven effective in accelerating the degradation of dyes and antibiotics in water. Additionally, CQDs serve as potent photosensitizers, expediting electron transfer, mitigating charge recombination, and bolstering light absorption efficiency [18–20]. Their small nanoparticle size, high biocompatibility, stability in water, easy functionalization, and robust fluorescence properties make them indispensable [21–23], with cost-effective production from readily available raw materials such as chitosan, grapefruit peel, sugarcane bagasse, and orange peel [24].

This study introduces a Z-scheme heterogeneous photocatalyst synthesized through the combination of Ag₃PO₄/GCN/FeNi-BTC (AGF) with CQDs extracted from shrimp shells. The synthesis process, conducted via a microwave-assisted hydrothermal method, emphasizes the use of environmentally friendly solvents to avoid toxic alternatives. The resulting AGF-CQD materials were then utilized as photocatalysts for the removal of tetracycline in water. A systematic investigation meticulously examined various factors affecting the tetracycline degradation process, including catalyst dosage, antibiotic concentration, pH levels, water source, reaction intermediates, and catalyst stability.

Materials and methods

Synthesis of Ag₃PO₄ sample

To synthesize the Ag₃PO₄ sample, slowly add 50 mL of 0.4 M Na₂HPO₄ into 50 mL of 1.2 M AgNO₃ solution and stir the mixture for 10 min at room temperature. Next, the yellow solid was separated by centrifugation and washed several times with water and ethanol. The obtained yellow Ag₃PO₄ material was then dried at 80 °C for 12 h.

Synthesis of GCN (g-C₃N₄) sample

The GCN material was synthesized from ammonium chloride and urea, using a thermal condensation method. Specifically, 10 g of ammonium chloride (NH₄Cl) and 10 g of urea ((NH₂)₂CO) were finely ground in a mortar before being placed in a porcelain dish with a melamine plate. This solid was heated at 550 °C for 3 h to obtain the GCN material.

Synthesis of Ag₃PO₄/GCN/FeNi-BTC and Ag₃PO₄/GCN/FeNi-BTC/CQD composites

Ag₃PO₄/GCN/FeNi-BTC (AGF) and Ag₃PO₄/GCN/FeNi-BTC/CQD (AGF-CQD) were synthesized using a microwave-assisted hydrothermal method. Specifically, 2.54 g of trimesic acid was dissolved in 60 mL of 1 M NaOH solution and stirred (500 rpm) to ensure complete dissolution (solution A). In parallel, 0.570 g of NiCl₂·6H₂O and 2.594 g of FeCl₃·6H₂O were dissolved in 60 mL of H₂O (solution B). Then, a mixture containing 0.8 g of GCN and m g of Ag₃PO₄ (m = 0.35, 0.788 and 1.352 g corresponding to 10 %AGF, 20 %AGF, and 30 %AGF samples) was dispersed into a colloidal solution in 60 mL of H₂O (solution

C). Next, solution B was slowly added to solution A, and the resulting mixture was stirred for 30 min. Then, solution C was slowly added to the mixture of solutions A and B, and stirred for another 30 min before being transferred to a Teflon bottle. The Teflon bottle was microwave hydrothermally treated for 30 min at 100 °C and was subsequently allowed to cool naturally to room temperature and filtered and washed with ethanol many times to obtain the AGF materials.

The obtained AGF was dispersed in a mixture of CQD, H₂O and C₂H₅OH in a ratio of 20 mL/80 mL/20 mL, respectively and subjected to microwave-assisted hydrothermal treatment for an additional 30 min. The resulting mixture was then separated by centrifugation, washed with ethanol, the solid remainder was dried at 80 °C for 12 h to receive the AGF-CQD materials. The synthesis process of 20 %AGF-CQD material via the microwave-assisted hydrothermal method is presented in Fig. S1.

Photocatalytic activity

The experiments evaluate the activity of the Ag₃PO₄, GCN, FeNi-BTC, AGF, and AGF-CQD photocatalysts under visible light irradiation, using a 300 W Xenon lamp as the light source and used a KG3 filter to filter UV rays emitted in Xenon lamps. In addition, the photocatalytic reaction system was controlled by circulating water for cooling to ensure a reaction temperature of 25 °C. Firstly, 30 mg of the photocatalyst was added to 100 mL of tetracycline solution (30 mg/L) and stirred in the dark for 60 min to allow the material to adsorb the tetracycline solution. Then, visible light irradiation was applied to the reaction system, and at 15-minute intervals, 2 mL of the reaction solution was extracted using a 0.22 µm foam filter to separate the photocatalyst from the solution. The post-reaction solutions were analyzed by UV-Vis spectroscopy at a wavelength of 360 nm to determine the concentration after the reaction [25]. The reaction efficiency of tetracycline degradation was calculated using the following Equation (1).

$$\%H = \frac{(C_0 - C_t)}{C_0} \times 100 \quad (1)$$

Where %H, C₀, C_t respectively represent the reaction efficiency, initial tetracycline concentration, and concentration at time t.

Various factors affecting the tetracycline degradation process were examined, including the catalyst dosage (0.1, 0.2, 0.3, 0.4, and 0.5 g/L), initial antibiotic concentration (10, 20, 30, 40, and 50 mg/L), pH value (3, 5, 6, 7, 9), anions (SO₄²⁻, HCO₃⁻, Cl⁻, and H₂PO₄⁻ with a concentration of 1 or 10 mM), water sources (To Lich River, Hong River, Nhue River, Tay Lake and Hoan Kiem Lake), reaction radicals, and stability. Furthermore, the recovered photocatalyst was evaluated for its reusability over five reaction cycles and the characteristic properties of the material after the reaction was examined.

To assess the generated radicals, electrons (e⁻), and holes (h⁺), 0.5 mL of *tert*-butanol (TBA), 1,4-benzoquinone (BQ), ammonium oxalate monohydrate (AO), and potassium dichromate (K₂Cr₂O₇) with a concentration of 1 M were added to the reaction system before the light irradiation process is observed [26]. The •OH and •O₂⁻ radicals were determined using the electron spin resonance (ESR) method with 5,5-dimethyl-1-pyrroline-N-oxide (DMPO) as the trapping agent [27].

Results and discussion

The X-ray diffraction (XRD) patterns of the Ag₃PO₄, FeNi-BTC, GCN, and AGF-CQD samples are presented in Fig. 1A. The XRD pattern of the GCN shows a broad peak at 2θ of 27.26° (002), which is characteristic of g-C₃N₄ [28–30]. The peaks at 2θ of 20.92° (110), 29.72° (200), 33.36° (210), 36.61° (211), 42.55° (220), and 47.86° (310), characteristic of the Ag₃PO₄ phase (ICSD 14000) [31–33]. The FeNi-BTC exhibits peaks at 2θ of 6.21°, 10.42°, 11.09°, 12.6°, 19.01°, 20.05° and 27.53° are related to the crystalline structure of Fe-BTC [34–36]. In the XRD

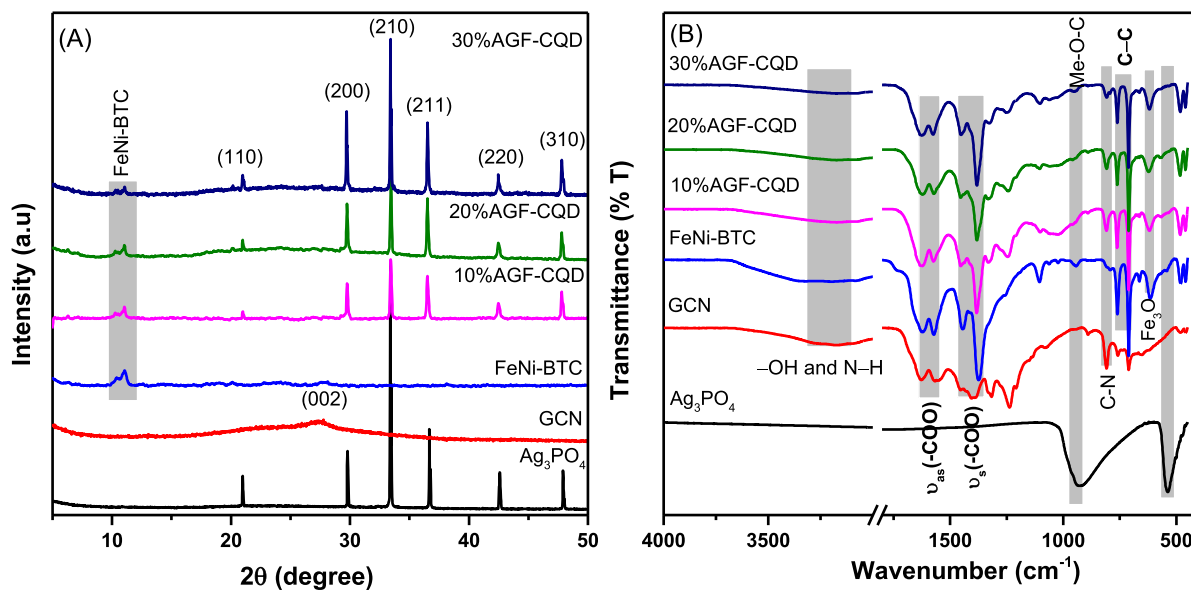


Fig. 1. (A) XRD patterns and (B) FT-IR spectra of Ag_3PO_4 , FeNi-BTC, GCN and AGF-CQD samples.

patterns of the AGF-CQD samples, all characteristic peaks of the Ag_3PO_4 and FeNi-BTC phases are observed (Fig. 1B). However, the characteristic peak of GCN is not observed, possibly due to overlapping with the peak of the FeNi-BTC [12]. The intensity of the characteristic peaks of Ag_3PO_4 significantly increases as the Ag_3PO_4 content increases from 10 to 30 wt %.

Fourier-transform infrared (FTIR) spectroscopy was used to observe changes in the chemical composition and functional groups in materials (Fig. 1B). The FTIR spectra of all samples show vibrational bands in the range of 3000–3600 cm⁻¹, which are assigned to the —OH groups on the surface of the characteristic —NH groups of the GCN. The Ag_3PO_4 material shows main vibrational bands at 950 and 560 cm⁻¹, which are assigned to the vibrational modes of the P—O bonds in PO_4^{3-} [37]. In addition, no vibrational bands of the Ag—O groups are observed because these vibrations do not absorb energy in the infrared region [7]. The aromatic C—N stretching vibrations (811, 1232, 1214, 1317, and 1459 cm⁻¹) and C≡N vibrations (1561 and 1627 cm⁻¹) of the GCN sample are observed in the FTIR spectrum [38]. The vibrational bands of the aromatic ring (756 and 712 cm⁻¹), Ni—O (660 cm⁻¹), C—O—Fe (1108 cm⁻¹), Fe₃O (612 cm⁻¹), and —COO⁻ groups (1626, 1565, 1374, and 1444 cm⁻¹) of the FeNi-BTC sample. In the AGF-CQD samples, the vibrational bands of the semiconductor materials Ag_3PO_4 , GCN, and Fe-NiBTC are observed. Furthermore, the characteristic vibrations of the carboxylic groups show a slight shift to higher wavenumbers by about 2–5 cm⁻¹, which is caused by the integration of the functional groups of CQD into the Ag_3PO_4 /Fe-NiBTC/GCN structure [39]. These results demonstrate the successful synthesis of the third-generation photocatalyst AGF-CQD.

The elemental composition of the Ag_3PO_4 , GCN, FeNi-BTC, and AGF-CQD samples was determined by energy-dispersive X-ray spectroscopy (EDS) and X-ray photoelectron spectroscopy (XPS) methods. The EDS spectroscopy shows characteristic peaks of the elements C, O, N, P, Fe, Ni, and Ag in the AGF-CQD samples. In Fig. S2, the intensity of the characteristic peaks of Ag and P significantly increases as the Ag_3PO_4 content increases from 10 to 30 wt%. Table S1 shows a slight decrease in the composition of the elements C, N, Fe, and Ni as the Ag_3PO_4 content increases from 10 to 30 wt%, while the content of Ag and P increases significantly. Table S2 presents the mole percentage composition of the elements in the 20 %AGF-CQD sample determined by EDS, which is similar to the composition determined by XPS (Table S3). The EDS-mapping images show a relatively even distribution of the elements C,

N, O, Fe, Ni, Ag, and P in the 20 %AGF-CQD sample (Fig. 2). During the synthesis of GCN, NH₄Cl acts as an interstitial agent, fostering conditions for the formation of nano GCN sheets. NH₄Cl is also readily decomposed at the synthesis temperature (500 °C) to release HCl and NH₃, explaining the absence of observed Cl in the XPS and EDS results [40].

Full scan survey XPS spectra of the Ag_3PO_4 , FeNi-BTC, GCN, and AGF-CQD samples are presented in Fig. S3. The XPS spectra of the AGF-CQD sample show the appearance of binding energies of C 1s (284 eV), O 1s (531 eV), P 2p (133 eV), N 1s (399 eV), Ag 3d (368 eV), Fe 2p (711 eV), and Ni 2p (856 eV).

For individual samples, characteristic peaks of the elements in the Ag_3PO_4 (Ag 3d, P 2p, and O 1s), GCN (N 1s, C 1s), and FeNi-BTC (C 1s, O 1s, Fe 2p, and Ni 2p) all appear in the full scan survey XPS spectra (Fig. S4). In high-resolution Ag 3d and O 1s XPS spectra of Ag_3PO_4 sample confirms the presence of Ag^+ (368.00 and 374.02 eV), lattice oxygen (O^{2-} , 530.67 eV), surface-adsorbed oxygen (532.47 eV), and P^{5+} (PO_4^{3-} , 133.07 eV) [41–43]. The elements Fe and Ni exist in the FeNi-BTC sample in the states of Fe^{2+} (710.89 and 723.53 eV), Fe^{3+} (713.51 and 725.65 eV), Ni^{2+} (856.13 and 873.94 eV), and Ni^{3+} (858.97 and 878.56 eV) as determined by high-resolution Fe 2p, Ni 2p, and O 1s XPS spectra. The C—C/C=C, C—O, C=O and O=C—O bonds with binding energies at 284.65, 285.85, 288.42, and 290.09 eV are observed in the high-resolution C 1s XPS spectra of the FeNi-BTC sample (Fig. 3). Additionally, the O=C—O, Me—O groups in the MOF network (Ni—O or Fe—O) exhibit binding energies at 531.13 and 531.80 eV, respectively, while the —OH group adsorbed on the surface is observed at 533.02 eV [5]. For the GCN sample, the C 1s XPS spectra reveal three peaks at 284.99, 286.51, and 288.29, corresponding to the C—C, C—N, and N—C≡N bonds, respectively [44]. The N 1s XPS spectra of the GCN have three peaks at binding energy levels of 398.85, 400.12, and 401.40 eV assigned to the sp^2N C—N=C bond, tertiary sp^3N nitrogen atom, and $\text{C}^2\text{—NH}$ amino group, respectively [45].

For the 20 %AGF-CQD sample, all characteristic peaks of C 1s, O 1s, N 1s, P 2p, Fe 2p, Ni 2p, and Ad 3d are fully observed (Table S4). However, it is possible to observe the binding energy shift of all elements in the 20 %AGF-CQD compared to the Ag_3PO_4 , FeNi-BTC, and GCN separately. Specifically, in the high-resolution XPS spectra of Ag 3d, Fe 2p, Ni 2p, O1s, and P 2p, the binding energy shift is observed in the positive direction, due to the decrease in electron density in the Ag_3PO_4 and FeNi-BTC phases [46]. Conversely, a clear energy shift towards the negative direction is observed for C 1s and N 1s in the GCN phase,

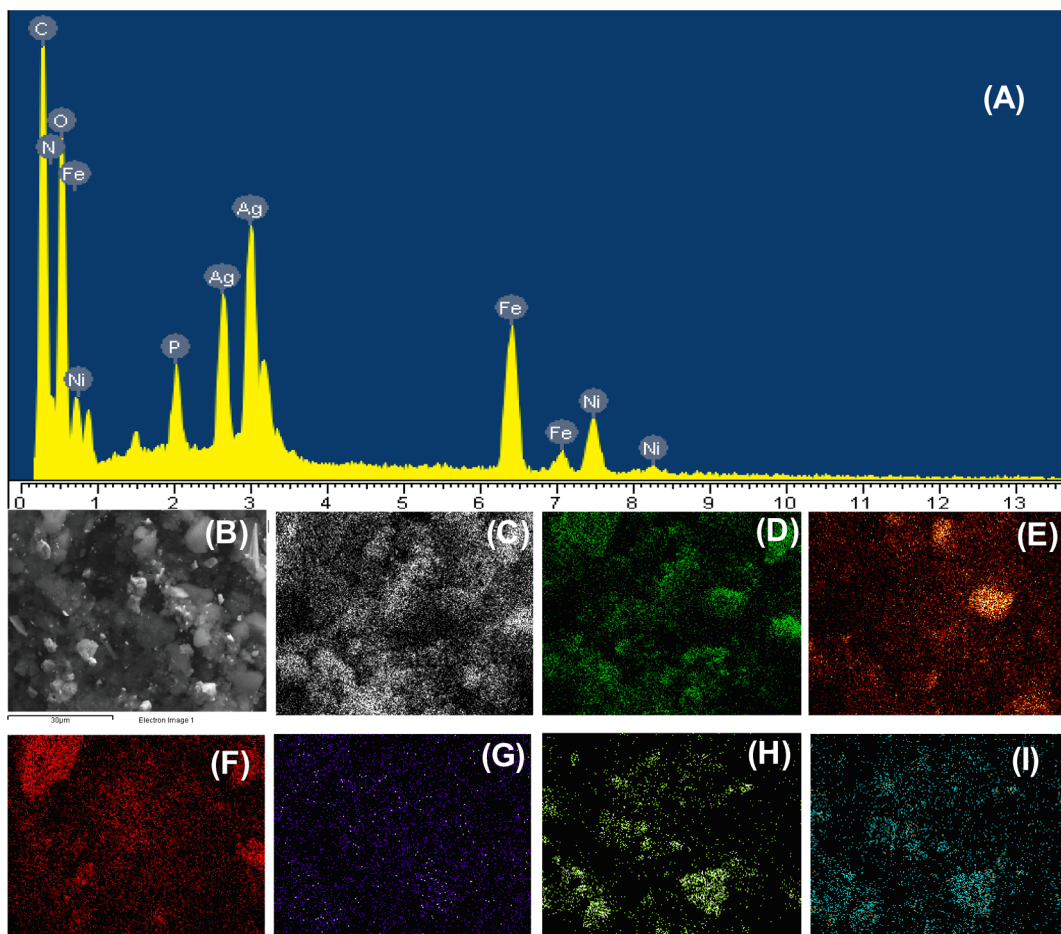


Fig. 2. EDS spectrum (A), EDS element layered image (B) EDS element mapping images of C (C), O (D), N (E), Fe (F), Ni (G), Ag (H), and P (I) of 20AGF-CQD sample.

resulting from the increase in electron density in the GCN phase structure [46,47]. Therefore, the formation of Me—N—O bonds (N—Fe—O) and the close contact between semiconductor materials through the interaction of CQD facilitate electron migration within the structure of the 20 %AGF-CQD. This observation elucidates the electron migration pathway in the structure of the 20 %AGF-CQD, wherein electrons traverse from the Ag_3PO_4 and FeNi-BTC phases through GCN via Me—N—O covalent bonds (N—Fe—O and N—Ni—O) and CQD [30,34,46],

The N_2 adsorption–desorption isotherms of Ag_3PO_4 , GCN, and AGF-CQD materials have a type IV shape, classified according to IUPAC (Fig. 4) [48]. At a relative pressure P/P_0 of about 0.8–1, a relatively wide hysteresis loop is observed, indicating the presence of a mesoporous structure. On the other hand, the N_2 adsorption–desorption isotherms of FeNi-BTC material belong to type I, which is commonly observed in microporous materials [49].

The specific surface areas of Ag_3PO_4 , GCN, and FeNi-BTC materials are 5.6, 87.9, and $1340 \text{ m}^2/\text{g}$, respectively. Therefore, the Ag_3PO_4 material has the lowest surface area ($5.6 \text{ m}^2/\text{g}$), while the FeNi-BTC sample has the highest surface area ($1340 \text{ m}^2/\text{g}$). For the AGF-CQD materials, a significant decrease in surface area and pore volume is observed, and this decrease is more pronounced as the Ag_3PO_4 content increases from 10 to 30 wt%. Specifically, the surface areas of 10 %AGF-CQD, 20 %AGF-CQD, and 30 %AGF-CQD materials are 945, 827, and $729 \text{ m}^2/\text{g}$, and the pore volumes are 1.109, 1.016, and $0.843 \text{ cm}^3/\text{g}$, respectively.

The morphology of Ag_3PO_4 , GCN, FeNi-BTC, and AGF-CQD materials was observed using scanning electron microscopy (SEM) and transmission electron microscopy (TEM) methods. Fig. S4A and C confirm that Ag_3PO_4 and FeNi-BTC materials have relatively uniform particle

sizes, measuring about 80–100 nm and 30–50 nm, respectively. In contrast, the GCN sample has a plate-like shape, with plate sizes ranging from 300–500 nm and non-uniform distribution. SEM images of AGF-CQD samples show that Ag_3PO_4 and FeNi-BTC clusters tend to aggregate together, while they are dispersed and evenly distributed on the GCN plate, rendering the observation of GCN plates challenging. The TEM images of Ag_3PO_4 , FeNi-BTC, GCN, and AGF-CQD materials are presented in Fig. 5. Fig. 5A shows the TEM image of Ag_3PO_4 with heterogeneous particle sizes, while GCN material showcases a plate-like structure (Fig. 5B). The FeNi-BTC sample has a spherical shape and uniform particle size (Fig. 5C). TEM images of AGF-CQD samples reveal bright-colored edges assigned to GCN and darker-colored particles assigned to nano Ag_3PO_4 and FeNi-BTC particles (Fig. 5D–F). Additionally, ultra-small 1–2 nm CQD nanoparticles are observed adorning the AGF heterogeneous catalyst. These TEM images validate the successful synthesis of AGF-CQD materials using the microwave-assisted hydrothermal method.

The optical and photoelectrochemical properties of Ag_3PO_4 , FeNi-BTC, GCN, and AGF-CQD materials are presented in Fig. 6. Fig. 6A shows the ultraviolet–visible diffuse Reflectance spectroscopy (UV-Vis DRS) of Ag_3PO_4 , FeNi-BTC, and GCN materials, revealing robust light absorption within the visible region. The band-gap energies (E_g) of Ag_3PO_4 , FeNi-BTC, and GCN materials are calculated to be 2.35, 2.67, and 2.74 eV, respectively, using the Tauc plot method [6]. Notably, upon amalgamating the semiconductor materials with carbon quantum dots, the light absorption intensity in the visible region significantly increases compared to the GCN sample [50].

This enhancement is attributed to the potent light absorption of Ag_3PO_4 and the quantum dot effect of CQD (AGF-CQD), combined with

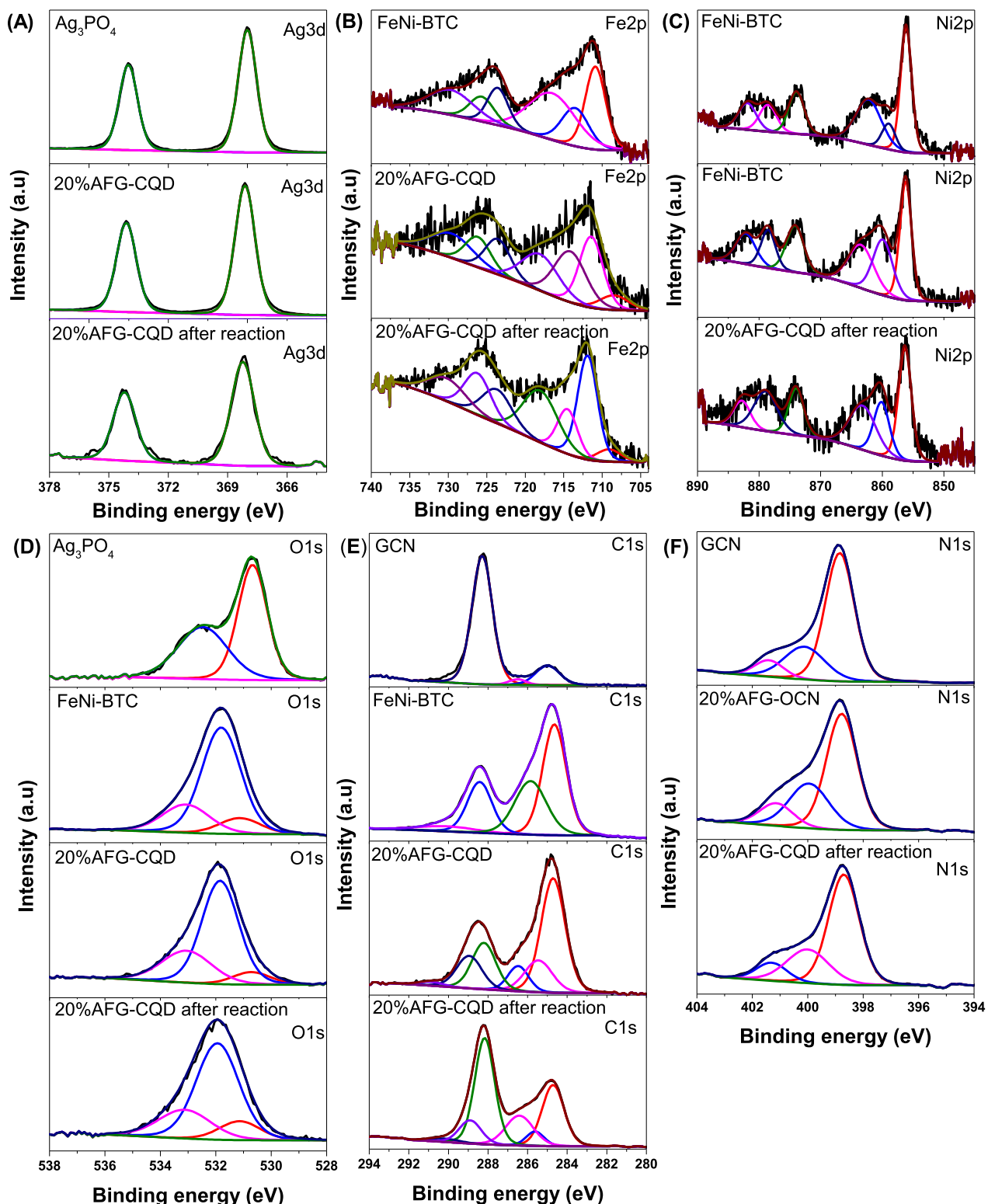


Fig. 3. High-resolution Ag 3d (A), Fe 2p (B), Ni 2p (C), O 1s (D), C 1s (E) and N 1s (F) XPS spectra of Ag_3PO_4 , FeNi-BTC, GCN, 20 %AFG-CQD before and after the reaction.

the direct formation of the Z-scheme heterojunction [51]. The bandgap energies of the 10 %AGF-CQD, 20 %AGF-CQD, and 30 %AGF-CQD samples are calculated to be 2.63, 2.56, and 2.48 eV, respectively (Fig. S5). Consequently, all materials exhibit the capacity to absorb light in the visible region, falling within the range of 2.35–2.74 eV, thereby promoting the generation of reactive species and augmenting the

photocatalytic reaction rate.

The Mott-Schottky plots were used to determine the flatband potential (E_{fb}) of Ag_3PO_4 , GCN, and FeNi-BTC materials. Fig. S6 confirms that Ag_3PO_4 , GCN, and FeNi-BTC materials are n-type semiconductors, as they have a negative slope, which is consistent with the report by Keke Chen and Xi Rao [46,52]. The flatband potentials of the Ag_3PO_4 ,

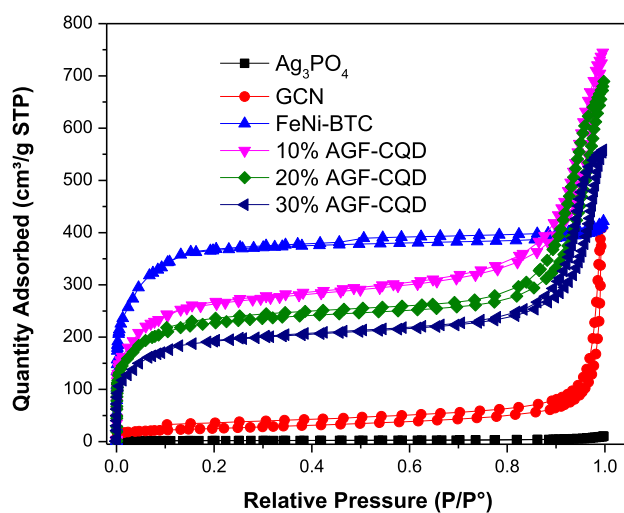


Fig. 4. N₂ adsorption–desorption isotherm of Ag₃PO₄, GCN, FeNi-BTC and AGF-CQD samples.

GCN, and FeNi-BTC samples are −0.26, −0.45 and −1.36 eV, respectively. The flatband potential can be referenced to the normal hydrogen electrode (NHE) based on Equation (2) using the flatband potential on the Ag/AgCl electrode.

$$E_{(NHE)} = E^\circ_{Ag/AgCl} + 0.059pH + E_{Ag/AgCl} \quad (2)$$

where E_{Ag/AgCl} is the working potential using Ag/AgCl (pH of 7.4) and E_{Ag/AgCl}° = 0.1976 eV at 25 °C.

The flat band potential (E_{fb}) of Ag₃PO₄, FeNiBTC, and GCN is determined according to equation (Eq. (2)) to be +0.37, +0.18, and −0.73 eV, respectively, relative to NHE. The valence band (VB) of the n-type semiconductor materials has a flat band width E_{fb} ranging from 0.1

or 0.2, so we choose it to be 0.2 eV. Therefore, the VB values of Ag₃PO₄, FeNiBTC, and GCN materials are 0.17, −0.02, and −0.93 eV, respectively. The CB positions of Ag₃PO₄, FeNi-BTC, and GCN can be identified based on the connection relationship the E_{VB} and E_g which are 2.52, 2.65, and 1.81 eV, respectively.

The electronic separation and transmission characteristics of e[−]/h⁺ pairs on Ag₃PO₄, GCN, FeNi-BTC, and AGF-CQD samples have been tested using the transient photocurrent response (TPCR) spectra. TPCR was measured from 0 to 390 s in 6 on/off cycles (Fig. 6B). In Fig. 6B, AGF-CQD samples had higher optical current density than individual FeNi-BTC, Ag₃PO₄, and GCN, possibly due to the interaction between GCN and MOF nanoparticles to create a synergistic effect of the materials phases [34]. Additionally, the addition of CQD accelerated the electronic transfer process, leading to a greater separation of electron-hole pairs [53–55].

The recombination of electrons and holes of the photocatalysts Ag₃PO₄, FeNi-BTC, GCN, and AGF-CQD was determined by the photoluminescence (PL) method. In Fig. 6C, all photocatalysts strongly absorb visible light (400–600 nm). The Ag₃PO₄, FeNi-BTC, and GCN samples have a very high fluorescence intensity in the visible region, as these materials are excited and strongly absorb visible light [56–59]. The GCN sample has the highest fluorescence intensity, with an emission wavelength of 460 nm due to the electron transfer process n-π* and the recombination of holes (h⁺) and electrons (e[−]) [34]. The PL fluorescence intensity of the samples decreases in the following order: GCN > Ag₃PO₄ > FeNi-BTC > 20 %AGF > 30 %AGF-CQD > 10 %AGF-CQD > 20 %AGF-CQD. Thus, the process of combining third-generation semiconductors with carbon quantum dots has inhibited the recombination process of e[−]/h⁺, leading to a significant decrease in PL intensity [60]. This result is due to the electron transfer between semiconducting materials, and the assistance of CQD inhibits the recombination process of e[−]/h⁺ [61]. The 20 %AGF-CQD sample has a lower fluorescence intensity compared to the 20 %AGF sample, as CQD increases the ability to transmit charge, supports the charge transfer process, and prevents electron

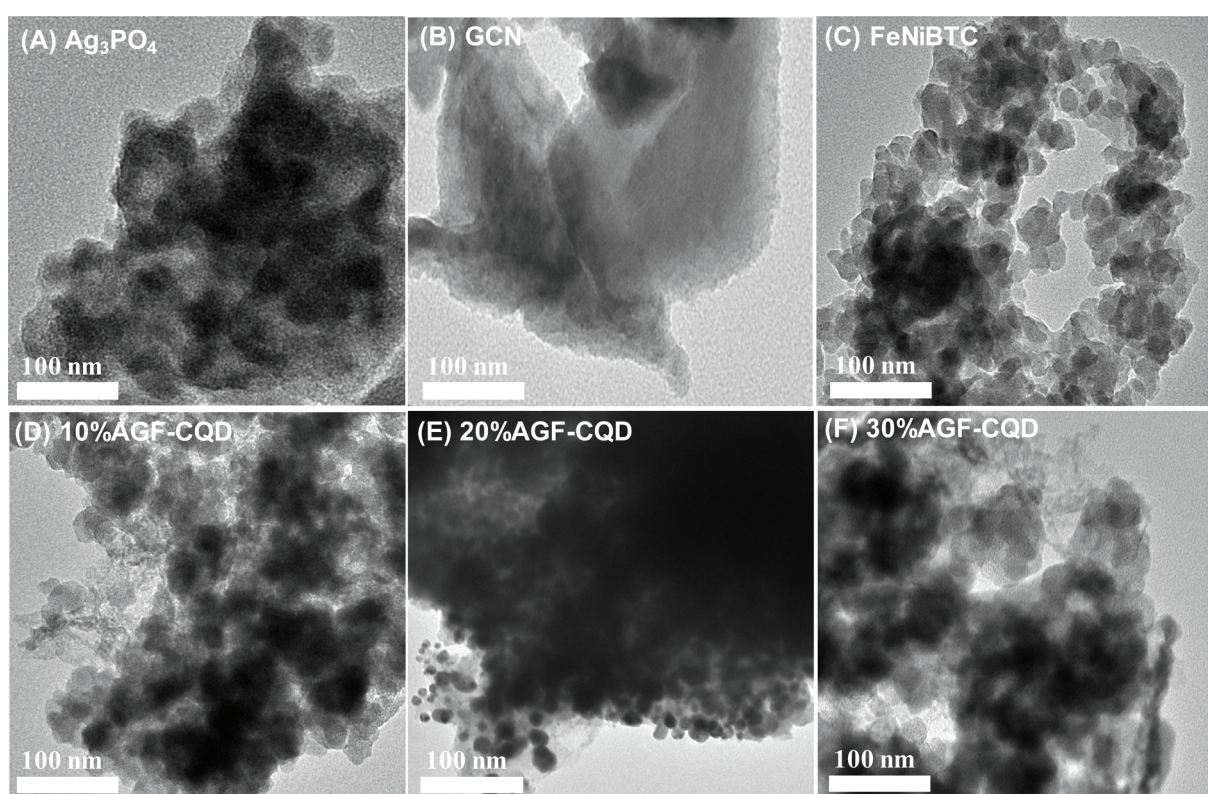


Fig. 5. TEM images of Ag₃PO₄, FeNi-BTC, GCN and AGF-CQD samples.

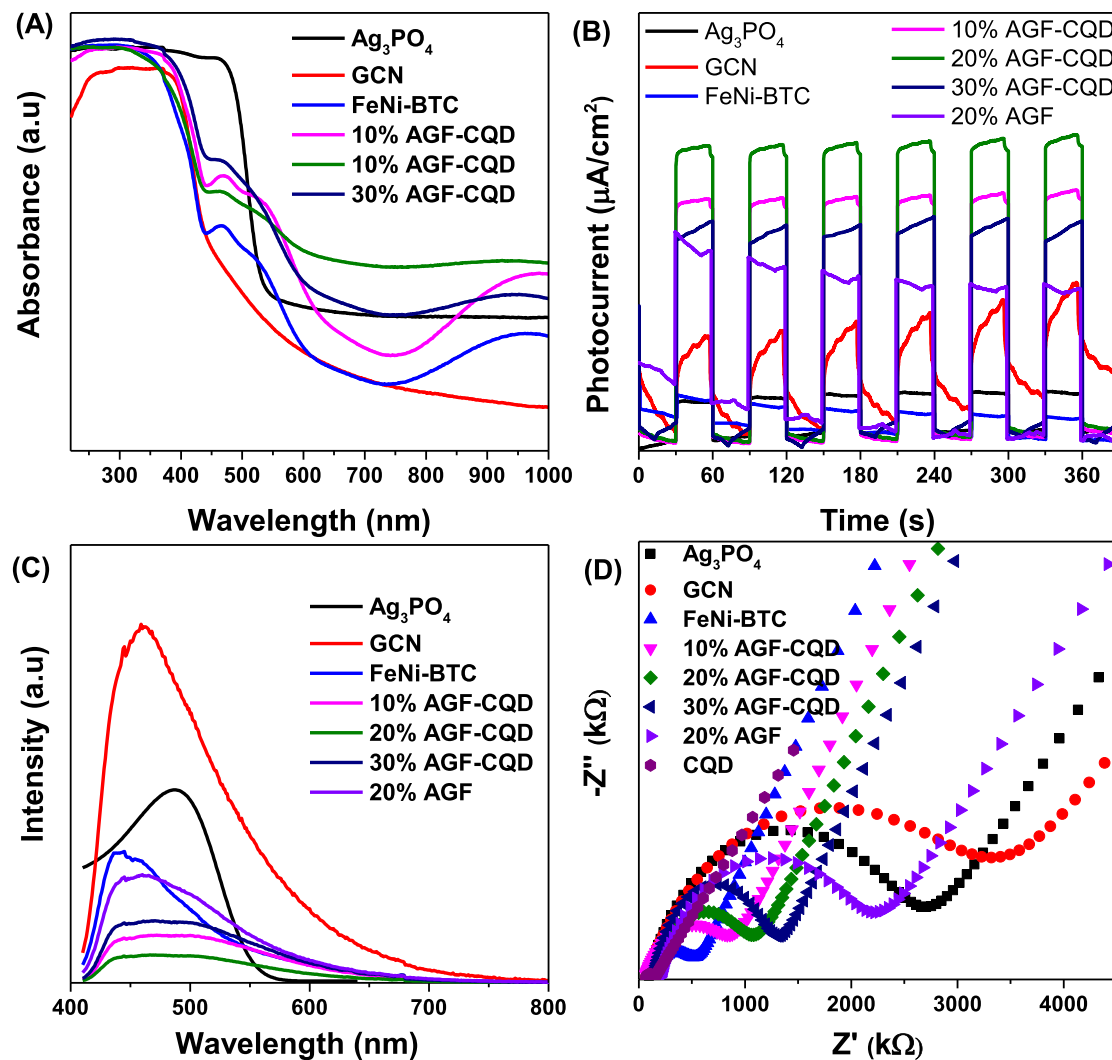


Fig. 6. (A) UV-Vis DRS spectra, (B) Transient photocurrent response, (C) Photoluminescence and (D) EIS of the Ag_3PO_4 , FeNi-BTC, GCN and AGF-CQD samples.

recombination [60].

The electrical charge transmission properties of the CQD, Ag_3PO_4 , GCN, FeNi-BTC, 20 %AGF and AGF-CQD samples were studied using electrochemical impedance spectroscopy (EIS). Fig. 6C shows that the Ag_3PO_4 , OCN, and 20 %AGF materials have very large semicircular shapes, confirming their slow electrical conductivity and charge transmission [62]. The CQD material has the best charge transmission and electrical conductivity due to its smallest semicircular diameter. The integration of CQD into the AGF materials has increased the speed of charge transmission and electrical conductivity. This result is attributed to the excellent electrical conductivity and charge transmission of CQD. For the AGF-CQD samples, as the Ag_3PO_4 content increases, the semicircular shape of the material increases, as Ag_3PO_4 has lower charge transmission capability. Thus, the synthesis of AGF-CQD samples has yielded advantageous properties for ion transportation and electrolyte diffusion, owing to their unique structures characterized by a high specific surface area that facilitates efficient charge transport [63]. The combination with CQD enhances strong interaction and close contact between components in the photocatalyst, creating favorable conditions for optimal electron transmission and minimal impedance [64]. Therefore, the prepared hybrid materials between AGF and CQD have achieved several advantages, including (i) enhanced visible light absorption ability (UV-Vis DRS); (ii) significantly improved electron transmission and separation processes, with shortened charge transmission distance,

which greatly reduces electronic recombination (PL and TPCR) [65].

Photocatalytic activity of Ag_3PO_4 , GCN, FeNi-BTC and AGF-CQD samples

The catalytic efficiency of Ag_3PO_4 , GCN, Fe-NiBTC, 20 %AGF, and AGF-CQD in the degradation of the tetracycline antibiotic was evaluated. In Fig. 7A, the Ag_3PO_4 , GCN, and Fe-NiBTC achieved tetracycline degradation efficiencies of 55.2 %, 73.5 %, and 81.3 % after 120 min, respectively. The Ag_3PO_4 and GCN had lower tetracycline treatment efficiency due to their low surface area (Table 1) and fast electron/hole recombination rate (Fig. 6C). The Fe-NiBTC sample with a high surface area ($1340 \text{ m}^2/\text{g}$), achieved the highest efficiency removal of tetracycline in the dark (52.18 %) due to the $\pi-\pi$ interaction between the benzene ring of the BTC³⁺ linker in FeNi-BTC and tetracycline [66].

However, the conduction band ($E_{\text{CB}} = -0.02 \text{ eV} > -0.33 \text{ eV}$) is insufficient to generate $\cdot\text{O}_2^-$ radicals, resulting in low photocatalytic activity (29.16 %). After combining the three semiconductor materials in AGF-CQD, the efficiency of tetracycline treatment significantly increases. Specifically, 10 %AGF-CQD, 20 %AGF-CQD, and 30 %AGF-CQD achieve 93.6 %, 98.1 %, and 96.5 % degradation of tetracycline after 105 min of reaction, respectively. However, exceeding the optimal Ag_3PO_4 level (30 %AGF-CQD) decreases the degradation efficiency of tetracycline from 98.1 % to 93.5 % due to reduced surface area, leading to decreased adsorption capacity and photocatalytic activity (Table 1).

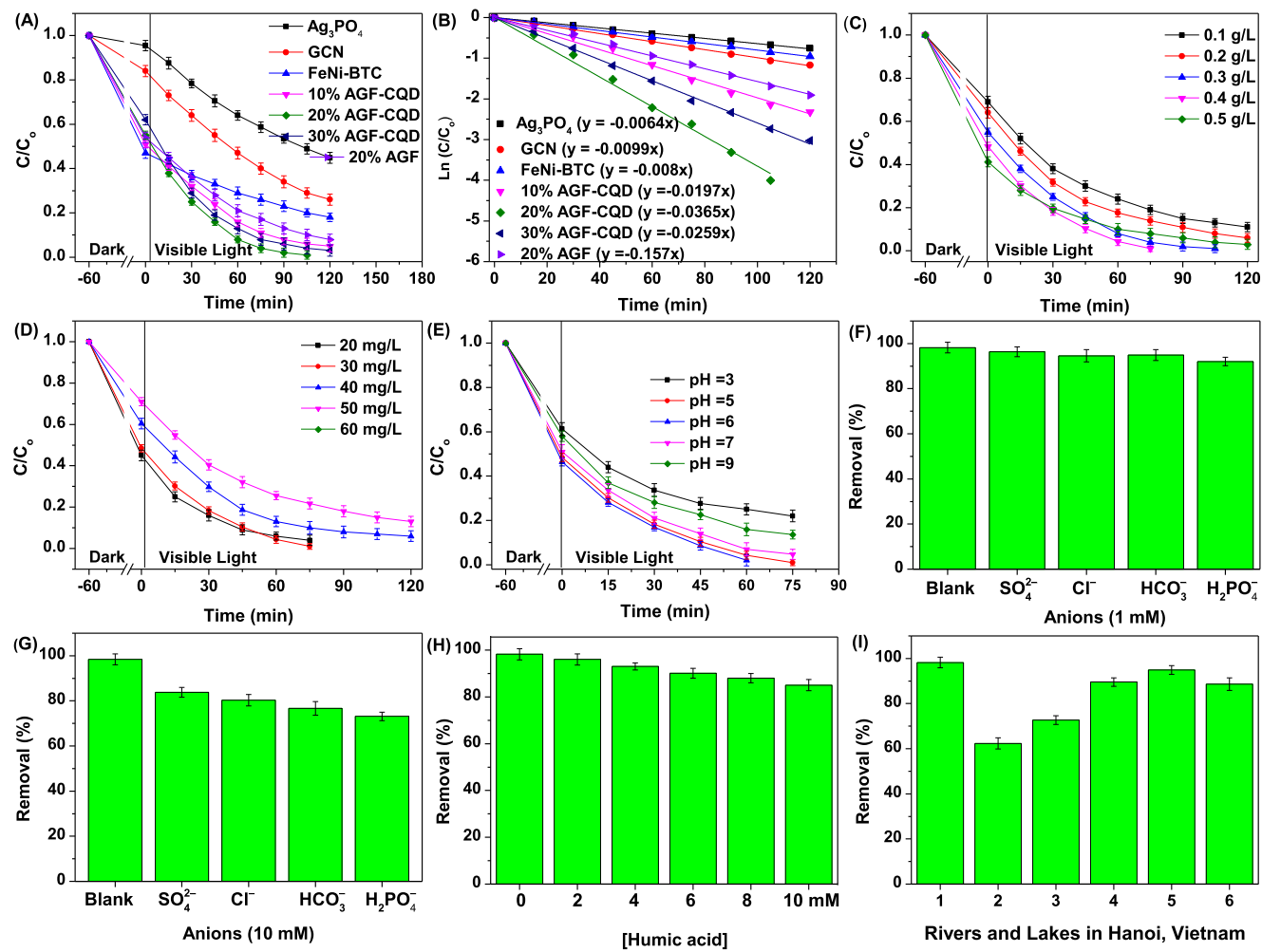


Fig. 7. (A) C/C_0 as a function of reaction time and (B) first-order reaction kinetics over Ag_3PO_4 , GCN, FeNi-BTC, 20 %AGF and AGF-CQD samples, C/C_0 as a function of reaction time over 20 %AGF-CQD with different photocatalyst amounts (C), tetracycline concentrations (D), pH value (E), anion 1 mM (F), anion 10 mM (G), humic acid concentrations (H) and different water sources in Hanoi (I).

Table 1

Surface area (S_{BET}), pore volume (V_{pore}) and pore diameter (D_{pore}) of Ag_3PO_4 , GCN, FeNi-BTC and AGF-CQD samples.

Samples	S_{BET} (m^2/g)	V_{pore} (cm^3/g)	D_{pore} (nm)	E_g (eV)
Ag_3PO_4	6.6	0.014	10.11	2.35
GCN	87.9	0.564	18.83	2.74
FeNi-BTC	1340	0.636	1.53	2.67
10 %AGF-CQD	945	1.109	4.75	2.63
20 %AGF-CQD	827	1.016	4.98	2.56
30 %AGF-CQD	729	0.843	5.29	2.28

Notably, the 20 %AGF-CQD sample (98.1 %) exhibits significantly higher tetracycline treatment efficiency compared to the 20 %AGF sample (89.8 %).

This enhancement can be due to CQD acting as a binding agent, enhancing the interaction between semiconductor materials, increasing the light absorption capacity, accelerating the speed of electrical transmission, and improving the efficiency of electron separation (Fig. 6B–D) [18]. Fig. 7B shows the reaction rate constants for the degradation of tetracycline by the photocatalysts Ag_3PO_4 , GCN, Fe-NiBTC, 10 %AGF-CQD, 20 %AGF-CQD, 30 %AGF-CQD, and 20 %AGF, which are 0.0064, 0.0099, 0.008, 0.0197, 0.0354, 0.0259, and 0.0157 min^{-1} , respectively. The reaction rate for the degradation of tetracycline by the 20 %AGF-CQD sample is 5.5, 3.6, 4.4, and 2.3 times faster than

that of the Ag_3PO_4 , GCN, Fe-NiBTC, and 20 %AGF samples, respectively. The 20 %AGF-CQD material was used to investigate the factors influencing the degradation process of tetracycline, such as the initial tetracycline concentration, the mass of the photocatalyst, pH, anion ions, and water source.

Different doses of the 20 %AGF-CQD, including 0.1, 0.2, 0.3, 0.4, and 0.5 g/L, were used to evaluate the effect of the dose of the catalyst on the efficiency of tetracycline treatment in water. Fig. 7C confirms that the dose of 20 %AGF-CQD has a significant impact on the efficient removal of tetracycline antibiotics. Specifically, increasing the dose of the photocatalyst 20 %AGF-CQD from 0.1 to 0.4 g/L resulted in an increase in the efficiency removal of tetracycline from 80.1 to 98.6 % after 75 min of visible light irradiation, due to the increase in the number of active sites [26]. However, increasing the amount of the catalyst is not always beneficial for the efficient removal of tetracycline antibiotics. Indeed, in the case of using a dose of 20 %AGF-CQD catalyst of 0.5 g/L (90.3 %), the amount of turbidity in the solution increased, leading to a decrease in the efficiency of visible light absorption, resulting in a decrease in the reduced separation between electrons and holes [67,68]. This observation aligns with findings reported by Nguyen, Pham and Ghasemipour et al. [6,26,69].

The 20 %AGF-CQD photocatalyst with a dosage of 0.4 g/L was used to study the initial tetracycline concentration, pH value, and the influence of the water source. Fig. 7D confirms that the initial tetracycline concentration affects the efficiency of the tetracycline treatment

process. When the tetracycline concentration increases from 20 to 30 mg/L, the efficiency removal of tetracycline does not change significantly. However, when the tetracycline concentration increases from 30 to 50 mg/L, the tetracycline degradation efficiency decreases from 98.6 % to 78.8 % after 75 min of visible light irradiation.

The degradation efficiency of tetracycline is greatly influenced by the pH of the initial solution, as the pH determines the surface charge of the catalyst and tetracycline [70]. In Fig. 7E, the removal efficiency of tetracycline increases from 74.5 % at pH = 3.0 to 98.4 % at pH = 6.0 and slightly decreases as the pH increases to 7 (95.2 %) and 9 (84.7 %), respectively. These results demonstrate that the 20 %AGF-CQD photocatalyst exhibits tetracycline degradation characteristics over a wide pH range [70]. At pH values < 3.3, tetracycline exists in fully protonated form with a positive charge, and 20 %AGF-CQD also carries a positive charge, so they repel each other. Furthermore, in a strong acid environment with excess H⁺ ions, they can interact with •OH radicals, inhibiting the tetracycline degradation process (Equation (3) [70].



At pH > 7.8, tetracycline carries a negative charge (TC⁻ and TC²⁻), and tetracycline also carries a negative charge. Because they have the same negative charge, causing them to repel each other at pH > 9, the degradation efficiency of tetracycline decreases [71,72]. At pH values of 5, 6, and 7, due to the positively charged catalyst surface electrostatically bonding with TC, one end of TC carries a negative charge, resulting in high TC treatment efficiency [72]. Therefore, at pH = 6, the 20 %AGF-CQD photocatalyst can treat 98.4 % of TC after 60 min of visible light irradiation.

The mineralization ability of the antibiotic tetracycline was analyzed in terms of total organic carbon (TOC), chemical oxygen demand (COD), and biological oxygen demand (BOD). The values of TOC, COD, and BOD after 60 min of reaction on the 20 %AGF-CQD photocatalyst reached 58.30 %, 77.90 %, and 81.08 %, respectively (Fig. S7). This result demonstrates that the heterogeneous photocatalyst AGF-CQD can mineralize tetracycline into CO₂, H₂O, and some inorganic compounds.

Fig. 7F confirms that the presence of anions at a concentration of 1 mM does not affect the degradation efficiency of tetracycline. The removal efficiency of tetracycline reaches over 92 % after 60 min of visible light irradiation. However, when the concentration of anions increases to 10 mM, the efficiency of tetracycline tends to decrease (Fig. 7G). Specifically, the presence of anions such as SO₄²⁻, Cl⁻, HCO₃⁻, and H₂PO₄⁻ leads to a decrease in the degradation efficiency of tetracycline from 98.4 % to 83.78 %, 80.31 %, 76.64 %, and 73.12 %, respectively. This result is due to the reaction radicals and vacancies generated during the reaction process combining with inorganic anions to form reaction radicals with lower activity [73]. The H₂PO₄⁻ anion inhibits the degradation reaction of tetracycline the most (78 %), and this phenomenon is the result of the quenching reaction of •OH and SO₄²⁻ radicals by H₂PO₄⁻.

For organic compounds humic acid (HA), the degradation efficiency of tetracycline decreases to 85 % due to the competitive reaction between tetracycline and HA, leading to a decrease in tetracycline degradation efficiency (Fig. 7H) [18]. Currently, antibiotics have appeared in ponds, rivers, and groundwater. Therefore, we collected some water sources from lakes, rivers, and hospital wastewater in Hanoi, Vietnam for research. The water sources include To Lich River, Hong River, Nhue River, Tay Lake, Hoan Kiem Lake, Bach Mai Hospital wastewater, and Viet Duc Hospital wastewater, which were collected, and solid particles were removed by filtration. Fig. 7I illustrates the significant difference in tetracycline treatment efficiency among different water sources in Hanoi (Vietnam). The difference is due to the diverse pollutants present in the lakes and rivers, which affect the water quality. For the Nhue River and To Lich River water sources, the tetracycline removal efficiency after 60 min reached 66.84 % and 71.35 %, respectively. The lower tetracycline treatment efficiency is related to the presence of suspended colloidal

substances and inorganic and organic pollutants, which hinder the absorption of visible light and directly compete with tetracycline [7,74]. The actual tetracycline treatment efficiency in Tay Lake (88.62 %), Hong River (94.90 %), and Hoan Kiem Lake (89.56 %) demonstrates the high practical application potential of the 20 % AGF-CQD photocatalyst.

Table S5 shows that different samples such as UiO-66-NDC/PC₃N₄, g-C₃N₄/UU-200, and β-Bi₂O₃/Ag₂O have been applied to treat tetracycline in water environments. The results indicate that the reported material systems effectively treat tetracycline, ranging from 72.6 % to 92.4 % removal after 120 to 180 min of reaction. In this study, under optimal conditions ([photocatalyst] = 0.4 g/L, [TC] = 30 mg/L, irradiation power of 300 W and pH = 6), the Ag₃PO₄/GCN/FeNi-BTC/CQD (20 % AGF-CQD) achieved 98.4 % tetracycline removal after 60 min of visible light irradiation. Table S5 shows that the amount of 20 % AGF-CQD photocatalyst used is less, but it achieves superior tetracycline removal compared to some previous publications. These results demonstrate that AGF-CQD material is a highly promising photocatalyst for the treatment of organic pollutants in the future.

Mechanism discussion

To better understand the photocatalytic mechanism of the AGF-CQD photocatalyst in the tetracycline treatment process, experiments to trap active radicals were conducted in Fig. 8. In Fig. 8A, the tetracycline treatment efficiency of the AGF-CQD photocatalyst reached 62.23 % when p-BQ was added to capture the •O₂⁻ radicals. When AO, IPA, and K₂Cr₂O₇ were successively added to the reaction system, the tetracycline treatment efficiencies were 72.56 %, 76.34 %, and 93.92 %, respectively after 60 min of visible light irradiation. Therefore, the roles of the reaction radicals in the degradation process of the antibiotic tetracycline are in the order of •O₂⁻ > h⁺ > •OH.

Electron spin resonance (ESR) was conducted using DMPO as an electron trap to determine the •O₂⁻ and •OH reaction radicals. In Fig. 8B, it is observed that the signal exhibits an intensity ratio of 1:2:2:1 for DMPO-•OH and a characteristic intensity ratio of 1:1:1:1 for DMPO-•O₂⁻ when exposed to visible light [34]. Conversely, these peak signals were not in the absence of light (in the dark). These results demonstrate the formation of •O₂⁻ and •OH radicals during the activation of the photocatalyst by visible light. Moreover, the signal of DMPO-•O₂⁻ is greater than that of DMPO-•OH in the AGF-CQD system, indicating a more significant role of •O₂⁻ radicals than •OH radicals [1].

In Fig. 9A, the conduction band (CB) energies of Ag₃PO₄ (0.17 eV) and FeNi-BTC (-0.02 eV) possess more positive reduction potential than that of E° O₂/[•]O₂⁻ = -0.33 eV, rendering the formation of •O₂⁻ radicals unfeasible in the conduction band of these semiconductors [34]. Conversely, the E_{CB} of GCN (-0.93 eV) exhibits a more negative reduction potential than that of E° O₂/[•]O₂⁻ = -0.33 eV, enabling the formation of •O₂⁻ radicals in the CB of GCN [36]. In the valence band (E_{VB}), GCN (1.81 eV) has a lower energy than the oxidation potential of E° H₂O/[•]OH (h⁺ + H₂O → •OH, E° H₂O/[•]OH = 2.40 eV), therefore precluding the formation of the •OH radicals in the CB of GCN. Conversely, due to the valence band energy of Ag₃PO₄ (2.52 eV) and FeNi-BTC (2.69 eV) being higher than the oxidation potential of E° H₂O/[•]OH (h⁺ + H₂O → •OH, E° H₂O/[•]OH = 2.40 eV), the •OH radicals can be generated in the CB of Ag₃PO₄ and FeNi-BTC. Based on the electrochemical properties and the roles of reaction radicals, we have proposed the band structure of AGF-CQD material (Fig. 9B). Firstly, the holes (h⁺) and electrons (e⁻) are excited by a light source with energy greater than 2.64 eV (Eq. (4)). Then, the electrons are separated and move to the conduction band (CB) and react with O₂ to form •O₂⁻ radicals (Eq. (5)).

Due to the strong bonding between semiconductors through the formation of Me—N and CQD bonds in GCF-CQD samples, electrons in the conduction band of Ag₃PO₄ and FeNi-BTC can easily move and recombine with the holes (h⁺) of GCN (Ag₃PO₄ → CQD → GCN and FeNi-BTC → CQD → GCN), (Eq. (6)). Next, under the influence of visible light,

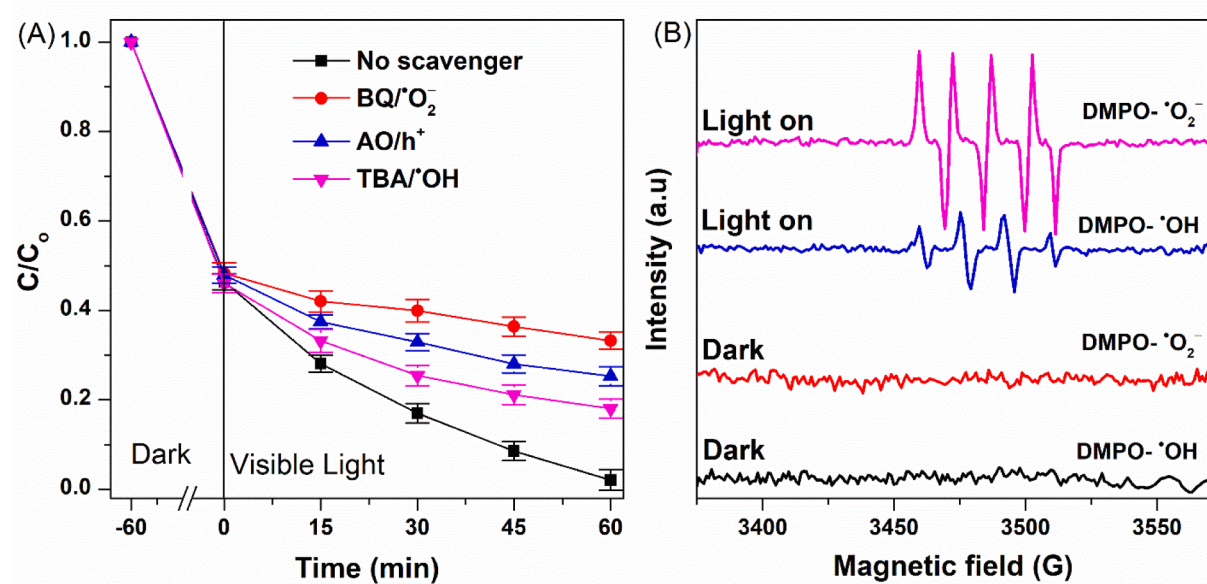


Fig. 8. (A) Reaction radical trap experiments and (B) ESR spectra for detecting $\cdot\text{OH}$ and $\cdot\text{O}_2^-$ on 20 %AGF-CQD.

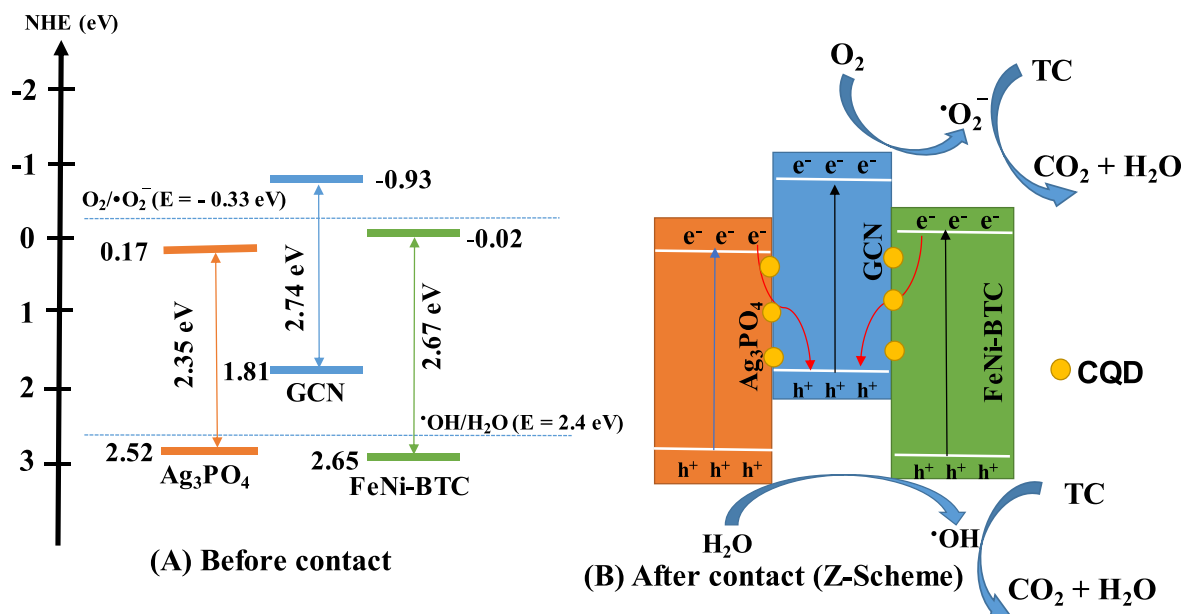
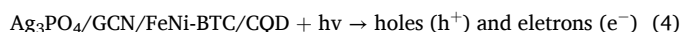


Fig. 9. Schematic illustration of separation and photo charge transfer on 20 %AGF-CQD sample before and after contact.

electrons (e⁻) and holes (h⁺) continue to separate to react with O₂ to generate $\cdot\text{O}_2^-$ radicals (Eq. (5)). In the valence band (VB), the valence band energy of Ag₃PO₄ (2.52 eV) and FeNi-BTC (2.65 eV) is higher than the energy of the H₂O/ $\cdot\text{OH}$ (2.4 eV), thus h⁺ reacts with $\cdot\text{OH}$ or H₂O absorbed on the surface to form $\cdot\text{OH}$ radicals (Eq. (7)).



Finally, the formed reaction radicals such as $\cdot\text{OH}$, $\cdot\text{O}_2^-$, and h⁺ oxidize tetracycline into less toxic products.

Analysis of photodegradation intermediates

Fig. S8 provides crucial insights into the degradation process of tetracycline in the presence of the 20 %AGF-CQD photocatalyst. A strong signal at *m/z* 445.14, characteristic of tetracycline, is initially observed in the solution. Over different reaction times, tetracycline gradually decomposes into smaller fragments, evidenced by the diminishing signal intensity of tetracycline. This decomposition is facilitated by $\cdot\text{OH}$, $\cdot\text{O}_2^-$ and h⁺ radicals, which possess strong oxidative properties and react with electron-rich groups in the tetracycline molecule, including phenolic hydroxyl groups, amino groups and double bonds. The degradation of tetracycline by the photocatalyst involves several reaction pathways, including acyl reduction, amine reduction, demethylation, water reduction, ring opening, hydroxylation, and mineralization [75].

First, tetracycline transforms into intermediate products such as T1 (*m/z* 415.18), T2 (*m/z* 461.26), T3 (*m/z* 358.12), T4 (*m/z* 383.05) and T5 (*m/z* 356.09) through methyl reduction, hydroxylation, deamination and dihydroxylation processes (Fig. 10). These intermediate compounds (T1-5) then undergo further ring-opening and hydroxylation reactions to form products like T6 (*m/z* 220.10), T7 (*m/z* 273.26), T8 (*m/z* 318.28), T9 (*m/z* 208.18), T10 (*m/z* 212.25), T11 (*m/z* 373.13), T12 (*m/z* 276.25) and T13 (*m/z* 258.16). Subsequently, these compounds are

oxidized through ring-opening reactions to form shorter fragments such as T14 (*m/z* 84.78), T15 (*m/z* 192.16), T16 (*m/z* 204.10), T17 (*m/z* 191.16), T18 (*m/z* 221.10), T19 (*m/z* 138.17), T20 (*m/z* 138.26), T21 (*m/z* 192.97), T22 (*m/z* 110.12), T23 (*m/z* 110.11). Next, Finally, these fragments are mineralized into short circuit products acids such as acetic acid (T25, *m/z* 60.08), succinic acid (T23, *m/z* 118.08), T24 (*m/z* 116.13), propionic acid (T27, *m/z* 74.13), malonic acid (T26, *m/z* 104.12), and eventually oxidized into inorganic products, CO₂, and H₂O

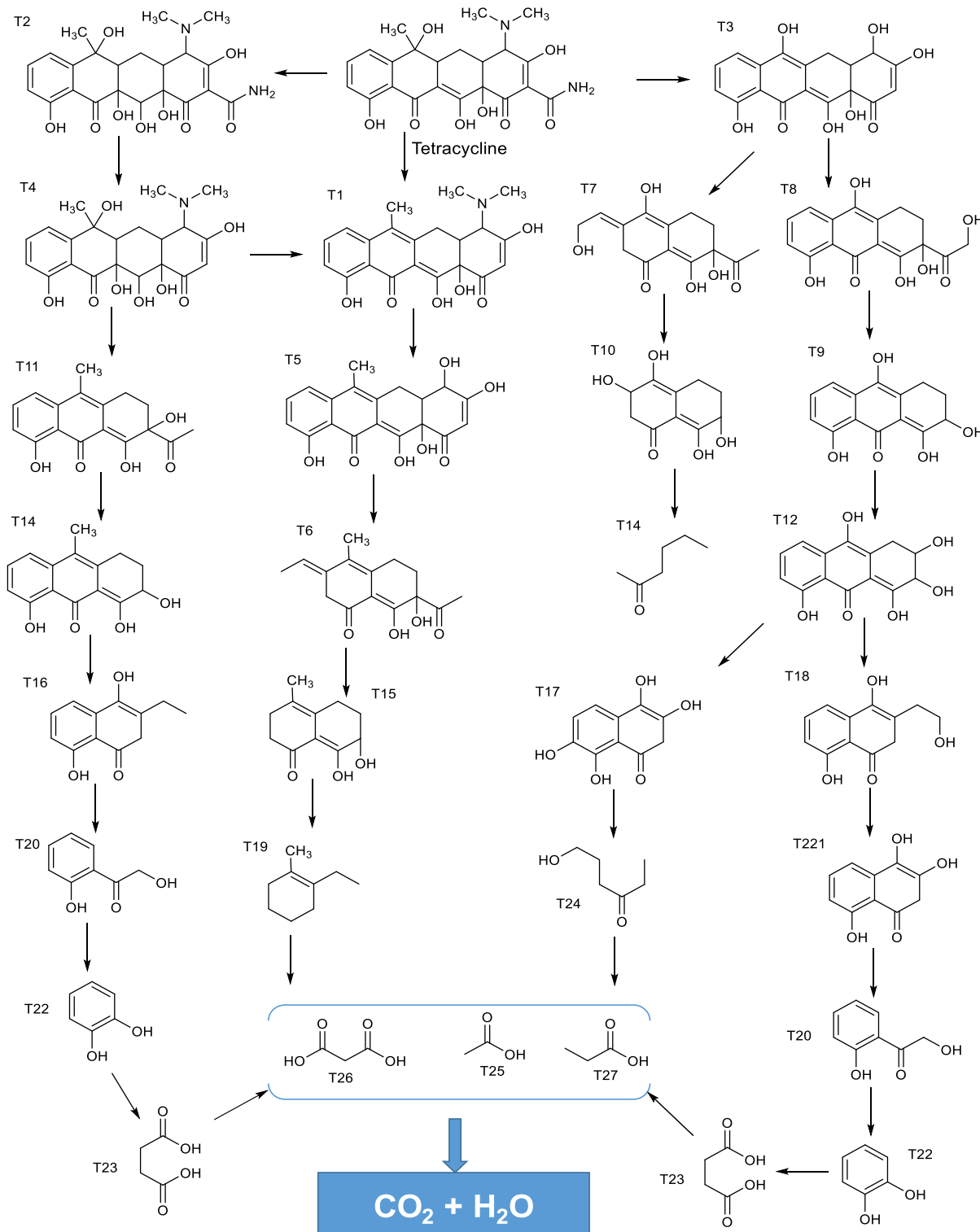


Fig. 10. Possible degradation pathways of tetracycline on 20 %AGF-CQD sample.

[76,77]. This comprehensive degradation pathway signifies the photocatalyst's ability to effectively break down TC into less harmful and simpler compounds, showcasing its potential for pollutant treatment in water environments.

Toxicity analysis of tetracycline degradation intermediates

The biological toxicity of the photocatalyst, along with the tetracycline product before and after the photocatalytic decomposition reaction on the 20 %AGC-CQD photocatalyst, was evaluated through the cultivation of green beans and monitoring the disinfection process *E. coli* bacteria. Initially, samples included tetracycline (30 mg/L), 20 %AGF-CQD photocatalyst at a concentration of 0.4 g/L, and the tetracycline solution after being treated with photocatalytic technology for 60 min, separated from the solid substance (catalyst) for use as a water source in the growth process of green beans and *E. coli* bacteria. In Fig. S9, tetracycline water sources (30 mg/L), tetracycline after treatment adversely affected the growth and development of mung beans. After 2 days of cultivation, the beans obtained in the tetracycline solution had short roots and stems and showed signs of damage. In contrast, beans cultivated in ion water sources, catalyst solution, and tetracycline water after treatment had larger and healthier stems and longer roots. This result indicates that the toxicity of the tetracycline decomposition solution is much lower than that of the original tetracycline solution. The effects of intermediate products after tetracycline decomposition have been studied on the gram-negative strain *E. coli* as a reference bacterium to investigate the effects of intermediate decomposition compounds. Agar disk-diffusion method is used to evaluate the impact of different types of water, including distilled water and tetracycline solution, on the growth of gram-negative bacteria *E. coli* [78]. The principle of this method is to determine the diffusion ability of the drug into the agar layer, which inhibits the growth of *E. coli* bacteria around the agar hole and larger the inhibitory zone, the stronger the effect of the drug. The TC solution (30 mg/L) inhibited the growth of *E. coli*, given its inherent antibacterial properties. On the other hand, the distilled water sample and the tetracycline solution after treatment showed rapid growth in the number of *E. coli* bacteria, indicating effective mitigation of tetracycline toxicity by the 20 %AGF-CQD photocatalyst.

Stability of 20 %AGF-CQD

The stability of the photocatalyst is an important factor determining the applicability of the catalyst in practice. The photocatalyst 20 %AGF-CQD is used in the photodegradation process of tetracycline in 5 different reaction cycles. Fig. S11 shows that the TC treatment efficiency reaches over 92 % after 5 reaction cycles. The XPS spectra of the 20 %AGF-CQD sample after 5 reaction cycles does not show any significant changes (Fig. 2). However, the characteristic binding energies of the elements have a positive energy shift, which is due to the loss of charge on the catalyst surface during the reaction [79]. TEM and XRD images (Figures S12 and S13) confirm that the structure of 20 %AGF-CQD does not show any significant changes. These results demonstrate that the 20 %AGF-CQD photocatalyst is highly efficient, stable, and promising for the treatment of organic compounds in water environments.

Conclusion

In this study, $\text{Ag}_3\text{PO}_4/\text{GCN}/\text{FeNi-BTC/CQD}$ photocatalyst was first synthesized using a green and environmentally friendly method, without the use of toxic solvents, and utilizing by-products of marine products. The AGF-CQD material possesses many outstanding advantages such as (i) strong visible light absorption and bandgap energy of 2.28–2.63 eV confirmed by UV-Vis DRS, (ii) efficient separation of electrons and holes confirmed by TPCR spectroscopy, (iii) efficient electron diffusion and transfer confirmed by EIS spectroscopy, and reduced charge recombination rate of holes and electrons confirmed by

PL spectroscopy.

Under optimal conditions ($[\text{photocatalyst}] = 0.4 \text{ g/L}$, $[\text{TC}] = 30 \text{ mg/L}$, irradiation power of 300 W, and $\text{pH} = 6$), the $\text{Ag}_3\text{PO}_4/\text{GCN}/\text{FeNi-BTC/CQD}$ material (20 % AGF-CQD) achieved 98.4 % tetracycline removal after 60 min of visible light irradiation. The degradation rate of tetracycline by $\text{Ag}_3\text{PO}_4/\text{GCN}/\text{FeNi-BTC/CQD}$ material is 5.5, 3.6, 4.4, and 2.3 times higher than that of Ag_3PO_4 , GCN, Fe-NiBTC, and 20 %AGF samples, respectively. The values of TOC, BOD, and COD after 60 min of reaction on the 20 %AGF-CQD photocatalyst reached 58.30 %, 77.90 %, and 81.08 % respectively. The roles of the reaction radicals in the degradation process of the antibiotic tetracycline are in the order of $\bullet\text{O}_2 > \text{h}^+ > \bullet\text{OH}$ confirmed by reactive radical trap experiments and ERS spectra.

CRediT authorship contribution statement

Manh B. Nguyen: Writing – review & editing, Writing – original draft, Visualization, Supervision, Software, Methodology, Investigation, Funding acquisition, Formal analysis, Data curation, Conceptualization. **Huan V. Doan:** Supervision, Methodology, Data curation, Conceptualization. **Doan Le Hoang Tan:** Writing – review & editing, Resources, Data curation, Conceptualization. **Tran Dai Lam:** Validation, Supervision, Methodology, Data curation.

Declaration of competing interest

The authors declare that they have no known competing financial interests or personal relationships that could have appeared to influence the work reported in this paper.

Acknowledgement

[Manh B. Nguyen] was funded by the Master, PhD Scholarship Programme of Vingroup Innovation Foundation (VINIF), code [VINIF.2023.TS.066].

Appendix A. Supplementary material

Supplementary data to this article can be found online at <https://doi.org/10.1016/j.jiec.2024.07.001>.

References

- [1] Y. Xie, C. Liu, D. Li, Y. Liu, In situ-generated H_2O_2 with NCQDs/MIL-101(Fe) by activating $\bullet\text{O}_2$: a dual effect of photocatalysis and photo-Fenton for efficient removal of tetracycline at natural pH, Appl. Surf. Sci. 592 (2022) 153312, <https://doi.org/10.1016/j.apsusc.2022.153312>.
- [2] W.Z. She, C.H. Li, R.S. Li, J. Ling, Q. Cao, Construction of two-dimensional fluorescent covalent organic framework nanospheres for the detection and removal of tetracycline, Sep. Purif. Technol. 330 (2024) 125294, <https://doi.org/10.1016/j.seppur.2023.125294>.
- [3] T.O. Ajiboye, L. Sawunyama, M.P. Ravele, A.A. Rasheed-Adeleke, N.H. Seheri, D. C. Onwudiwe, S.D. Mhlanga, Synthesis approaches to ceramic membranes, their composites, and application in the removal of tetracycline from water, Environ. Adv. 12 (2023) 100371, <https://doi.org/10.1016/j.envadv.2023.100371>.
- [4] M.A. Ahmed, M.A. Ahmed, A.A. Mohamed, Adsorptive removal of tetracycline antibiotic onto magnetic graphene oxide nanocomposite modified with polyvinylpyrrolidone, React. Funct. Polym. 191 (2023) 105701, <https://doi.org/10.1016/j.reactfunctpolym.2023.105701>.
- [5] M.B. Nguyen, G.H. Le, T. Duy, Q.K. Nguyen, T. Trang, T. Pham, T. Lee, T.A. Vu, Bimetallic Ag-Zn-BTC/GO composite as highly efficient photocatalyst in the photocatalytic degradation of reactive yellow 145 dye in water, J. Hazard. Mater. 420 (2021) 126560, <https://doi.org/10.1016/j.jhazmat.2021.126560>.
- [6] M.B. Nguyen, D.T. Sy, V.T.K. Thoa, N.T. Hong, H.V. Doan, Bimetallic Co-Fe-BTC/CN nanocomposite synthesised via a microwave-assisted hydrothermal method for highly efficient Reactive Yellow 145 dye photodegradation, J. Taiwan Inst. Chem. Eng. 140 (2022) 104543, <https://doi.org/10.1016/j.jtice.2022.104543>.
- [7] G.T.T. Pham, H.T. Vu, T.T. Pham, N.N. Thanh, V.N. Thuy, H.Q. Tran, H.V. Doan, M. B. Nguyen, Exploring the potential of $\text{ZnO}-\text{Ag}@\text{AgBr}/\text{SBA-15}$ Z-scheme heterostructure for efficient wastewater treatment: synthesis, characterization, and real-world applications, RSC Adv. 13 (2023) 12402–12410, <https://doi.org/10.1039/d3ra01856c>.

- [8] N. El Messaoudi, Z. Ciğeroğlu, Z.M. Şenol, M. Elhajam, L. Noureen, A comparative review of the adsorption and photocatalytic degradation of tetracycline in aquatic environment by g-C₃N₄-based materials, *J. Water Process Eng.* 55 (2023) 104150, <https://doi.org/10.1016/j.jwpe.2023.104150>.
- [9] W.J. Ong, L.L. Tan, Y.H. Ng, S.T. Yong, S.P. Chai, Graphitic carbon nitride (g-C₃N₄)-based photocatalysts for artificial photosynthesis and environmental remediation: are we a step closer to achieving sustainability? *Chem. Rev.* 116 (2016) 7159–7329, <https://doi.org/10.1021/acs.chemrev.6b00075>.
- [10] L. Xie, Z. Yang, W. Xiong, Y. Zhou, J. Cao, Y. Peng, X. Li, C. Zhou, R. Xu, Y. Zhang, Construction of MIL-53(Fe) metal-organic framework modified by silver phosphate nanoparticles as a novel Z-scheme photocatalyst: visible-light photocatalytic performance and mechanism investigation, *Appl. Surf. Sci.* 465 (2019) 103–115, <https://doi.org/10.1016/j.apsusc.2018.09.144>.
- [11] J. Xu, J. Xu, S. Jiang, Y. Cao, K. Xu, Q. Zhang, L. Wang, Facile synthesis of a novel Ag₃PO₄/MIL-100(Fe) Z-scheme photocatalyst for enhancing tetracycline degradation under visible light, *Environ. Sci. Pollut. Res.* 27 (2020) 37839–37851, <https://doi.org/10.1007/s11356-020-09903-w>.
- [12] M.B. Nguyen, H.V. Doan, D. Le, H. Tan, T. Dai, Advanced g-C₃N₄ and bimetallic FeNi-BTC integration with carbon quantum dots for removal of microplastics and antibiotics in aqueous environments, *J. Environ. Chem. Eng.* 12 (2024) 112965, <https://doi.org/10.1016/j.jece.2024.112965>.
- [13] A. Vijeata, A. Garg, G. Ram Chaudhary, S. Chaudhary, A. Bhalla, Nanocatalytic and antimicrobial potency of CQD@Pd nanoparticles: experimental and theoretical approach, *Appl. Surf. Sci.* 653 (2024) 159394, <https://doi.org/10.1016/j.apsusc.2024.159394>.
- [14] M.E. Khan, A. Mohammad, T. Yoon, State-of-the-art developments in carbon quantum dots (CQDs): photo-catalysis, bio-imaging, and bio-sensing applications, *Chemosphere* 302 (2022) 134815, <https://doi.org/10.1016/j.chemosphere.2022.134815>.
- [15] W.C. Hsiao, C.H. Tseng, C.W. Huang, A facile reflux method to produce ternary CQDs/P25/NH₂-MIL-125 for photocatalytic degradation of methylene blue under simulated solar light, *J. Taiwan Inst. Chem. Eng.* 154 (2024) 105286, <https://doi.org/10.1016/j.jtice.2023.105286>.
- [16] S. Lv, Y. Li, K. Zhang, Z. Lin, D. Tang, Carbon Dots/g-C₃N₄ nanoheterostructures-based signal-generation tags for photoelectrochemical immunoassay of cancer biomarkers coupling with copper nanoclusters, *(2017)* 38336–38343, doi: 10.1021/acsmami.7b13272.
- [17] J. Li, B. Zhang, J. Lu, Z. Guo, M. Zhang, D. Li, Z. Zhao, S. Song, Y. Liu, L. Qin, A CQD/Cds/g-C₃N₄ photocatalyst for dye and antibiotic degradation: dual carrier driving force and tunable electron transfer pathway, *Sep. Purif. Technol.* 305 (2023) 122333, <https://doi.org/10.1016/j.seppur.2022.122333>.
- [18] H. Jiang, Y. Zhong, K. Tian, H. Pang, Y. Hao, Enhanced photocatalytic degradation of bisphenol A over N, S-doped carbon quantum dot-modified MIL-101(Fe) heterostructure composites under visible light irradiation by persulfate, *Appl. Surf. Sci.* 577 (2022) 151902, <https://doi.org/10.1016/j.apsusc.2021.151902>.
- [19] D.L. Zhao, H. Jin, Q. Zhao, Y. Xu, L. Shen, H. Lin, T.S. Chung, Smart integration of MOFs and CQDs to fabricate defect-free and self-cleaning TPN membranes for dye removal, *J. Membr. Sci.* 679 (2023) 121706, <https://doi.org/10.1016/j.memsci.2023.121706>.
- [20] J. Zhang, R. Liu, M. Kuang, S. Xie, J. Wang, Z. Ji, Constructing CQDs/MIL-101(Fe)/g-C₃N₄ photocatalyst and its enhancement to the photocatalytic activity, *Mater. Lett.* 101 (2023) 135004, <https://doi.org/10.1016/j.matlet.2023.135004>.
- [21] H. Teymourinia, H.A. Alshamsi, A. Al-nayili, E. Sohouli, M. Gholami, Synthesis of new photocatalyst based on g-C₃N₄/N, P CQD/ZIF-67 nanocomposite for ciprofloxacin degradation under visible light irradiation, *J. Ind. Eng. Chem.* 125 (2023) 259–268, <https://doi.org/10.1016/j.jiec.2023.05.035>.
- [22] A. Kumar, S.K. Sharma, G. Sharma, M. Naushad, F.J. Stadler, CeO₂/g-C₃N₄/V₂O₅ ternary nano hetero-structures decorated with CQDs for enhanced photo-reduction capabilities under different light sources: dual Z-scheme mechanism, *J. Alloys Compd.* 838 (2020) 155692, <https://doi.org/10.1016/j.jallcom.2020.155692>.
- [23] S. Li, X. Liu, Y. Zheng, J. Ma, S. You, H. Zheng, Effective peroxydisulfate activation by CQDs-MnFe₂O₄@ZIF-8 catalyst for complementary degradation of bisphenol A by free radicals and non-radical pathways, *Chin. Chem. Lett.* (2023) 108971, <https://doi.org/10.1016/j.ccl.2023.108971>.
- [24] H. Chai, Z. Zhang, J. Sun, M. Zhong, M. Liu, J. Li, Z. Chen, B. Gong, Q. Xu, Z. Huang, L. Cui, Enhancing tetracycline degradation with biomass carbon quantum dot (CQDs)-modified magnetic heterojunction CeO₂-Fe₃O₄ under visible light, *J. Environ. Chem. Eng.* 12 (2024) 112338, <https://doi.org/10.1016/j.jece.2024.112338>.
- [25] M.M. Soori, E. Ghahramani, H. Kazemian, T.J. Al-Musawi, M. Zarrabi, Intercalation of tetracycline in nano sheet layered double hydroxide: an insight into UV/VIS spectra analysis, *J. Taiwan Inst. Chem. Eng.* 63 (2016) 271–285, <https://doi.org/10.1016/j.jtice.2016.03.015>.
- [26] X.N. Pham, H.T. Nguyen, T.N. Pham, T.T.B. Nguyen, M.B. Nguyen, V.T.T. Tran, H. V. Doan, Green synthesis of H-ZSM-5 zeolite-anchored O-doped g-C₃N₄ for photodegradation of Reactive Red 195 (RR 195) under solar light, *J. Taiwan Inst. Chem. Eng.* 114 (2020) 91–102, <https://doi.org/10.1016/j.jtice.2020.09.018>.
- [27] A. Kumar, S.K. Sharma, G. Sharma, A.H. Al-Muhtaseb, M. Naushad, A.A. Ghafar, F. J. Stadler, Wide spectral degradation of Norfloxacin by Ag@BiPO₄/BiOBr/BiFeO₃ nano-assembly: elucidating the photocatalytic mechanism under different light sources, *J. Hazard. Mater.* 364 (2019) 429–440, <https://doi.org/10.1016/j.jhazmat.2018.10.060>.
- [28] S. Hu, F. Li, Z. Fan, F. Wang, Y. Zhao, Z. Lv, Band gap-tunable potassium doped graphitic carbon nitride with enhanced mineralization ability, *Dalton Trans.* 44 (2014) 1084–1092, <https://doi.org/10.1039/c4dt02658f>.
- [29] S. Hu, L. Ma, J. You, F. Li, Z. Fan, G. Lu, D. Liu, J. Gui, Enhanced visible light photocatalytic performance of g-C₃N₄ photocatalysts co-doped with iron and phosphorus, *Appl. Surf. Sci.* 311 (2014) 164–171, <https://doi.org/10.1016/j.apusc.2014.05.036>.
- [30] M.B. Nguyen, P.T. Lan, N.T. Anh, N.N. Tung, S. Guan, V.P. Ting, T.T.B. Nguyen, H. V. Doan, M.T. Tung, T.D. Lam, Ternary heterogeneous Z-scheme photocatalyst TiO₂/CuInS₂/OCN incorporated with carbon quantum dots (CQDs) for enhanced photocatalytic degradation efficiency of reactive yellow 145 dye in water, *RSC Adv.* 13 (2023) 35339–35348, <https://doi.org/10.1039/d3ra07546j>.
- [31] P. Zhu, J. Lin, L. Xie, M. Duan, D. Chen, D. Luo, Y. Wu, Visible light response photocatalytic performance of Z-scheme Ag₃PO₄/GO/UiO-66-NH₂ photocatalysts for the levofloxacin hydrochloride, *Langmuir* 37 (2021) 13309–13321, <https://doi.org/10.1021/acs.langmuir.1c01901>.
- [32] P. Zhu, J. Lin, M. Liu, M. Duan, D. Luo, X. Wu, S. Zhang, Nd₂Sn₂O₇/Bi₂Sn₂O₇/Ag₃PO₄ double Z-type heterojunction for antibiotic photodegradation under visible light irradiation: mechanism, optimization and pathways, *Sep. Purif. Technol.* 300 (2022) 121897, <https://doi.org/10.1016/j.seppur.2022.121897>.
- [33] P. Zhu, Y. Chen, M. Duan, Z. Ren, M. Hu, Construction and mechanism of a highly efficient and stable Z-scheme Ag₃PO₄/reduced graphene oxide/Bi₂MoO₆ visible-light photocatalyst, *Cat. Sci. Technol.* 8 (2018) 3818–3832, <https://doi.org/10.1039/c8cy01087k>.
- [34] M.B. Nguyen, L.H.T. Nguyen, M.T. Le, N.Q. Tran, N.H.T. Tran, P.H. Tran, A.T. T. Pham, L.D. Tran, T.L.H. Doan, Engineering direct Z-scheme GCN/bimetallic-MOF heterojunctions as efficient and recyclable photocatalysts for enhancing degradation of RR 195 under visible light, *J. Ind. Eng. Chem.* 134 (2024) 217–230, <https://doi.org/10.1016/j.jiec.2023.12.052>.
- [35] A.R. Oveisi, A. Khorrababadi-Zad, S. Daliran, Iron-based metal-organic framework, Fe(BTC): an effective dual-functional catalyst for oxidative cyclization of bisnaphthols and tandem synthesis of quinazolin-4(3H)-ones, *RSC Adv.* 6 (2016) 1136–1142, <https://doi.org/10.1039/c5ra19013d>.
- [36] H.T. Vu, G.T.T. Pham, T.L.H. Doan, T.D. Lam, N.T. Van, N. Van Manh, P.T. Quyen, N.D. Hai, H.V. Doan, M.B. Nguyen, Influence of metal ions (Me: Fe, Cu Co, Ni, Mn, Cr) on direct Z-scheme photocatalysts CN/Me-BTC on the degradation efficiency of tetracycline in water environment, *J. Taiwan Inst. Chem. Eng.* 161 (2024) 105518, <https://doi.org/10.1016/j.jtice.2024.105518>.
- [37] X. Zhang, C. Chen, C. Jiang, H. Zhou, W. Cao, Y. Wang, Construction and mechanism of Ag₃PO₄/UiO-66-NH₂ Z-scheme heterojunction with enhanced photocatalytic activity, *Catal. Lett.* 151 (2021) 734–747, <https://doi.org/10.1007/s10562-020-03349-y>.
- [38] M. Tian, X. Ren, S. Ding, N. Fu, Y. Wei, Z. Yang, X. Yao, Effective degradation of phenol by activating PMS with bimetallic Mo and Ni Co-doped g-C₃N₄ composite catalyst: a Fenton-like degradation process promoted by non-free radical $\cdot\text{O}_2$, *Environ. Res.* 243 (2024) 117848, <https://doi.org/10.1016/j.envres.2023.117848>.
- [39] N.A. Travlou, M. Algarra, C. Alcoholoado, M. Cifuentes-Rueda, A.M. Labella, J. M. Lazaro-Martinez, E. Rodriguez-Castellon, T.J. Bandosz, Carbon quantum dot surface-chemistry-dependent Ag release governs the high antibacterial activity of Ag-metal-organic framework composites, *ACS Appl. Bio Mater.* 1 (2018) 693–707, <https://doi.org/10.1021/acsbm.8b00166>.
- [40] X. Wu, D. Gao, P. Wang, H. Yu, J. Yu, NH4Cl-induced low-temperature formation of nitrogen-rich g-C₃N₄ nanosheets with improved photocatalytic hydrogen evolution, *Carbon* 153 (2019) 757–766, <https://doi.org/10.1016/j.carbon.2019.07.083>.
- [41] M. Al Kausor, D. Chakrabortty, Optimization of system parameters and kinetic study of photocatalytic degradation of toxic acid blue 25 dye by Ag₃PO₄@RGO nanocomposite, *J. Nanopart. Res.* 22 (2020), <https://doi.org/10.1007/s11051-020-04829-3>.
- [42] M. Hu, P. Zhu, M. Liu, J. Xu, M. Duan, J. Lin, Preparation, performance and mechanism of p-Ag₃PO₄/n-ZnO/C heterojunction with IRMOF-3 as precursor for efficient photodegradation of norfloxacin, *Colloids Surf. A Physicochem. Eng. Asp.* 628 (2021) 127235, <https://doi.org/10.1016/j.colsurfa.2021.127235>.
- [43] Y. Chen, P. Zhu, M. Duan, J. Li, Z. Ren, P. Wang, Fabrication of a magnetically separable and dual Z-scheme PANI/Ag₃PO₄/NiFe₂O₄ composite with enhanced visible-light photocatalytic activity for organic pollutant elimination, *Appl. Surf. Sci.* 486 (2019) 198–211, <https://doi.org/10.1016/j.apsusc.2019.04.232>.
- [44] J. Cao, C. Qin, Y. Wang, H. Zhang, G. Sun, Z. Zhang, Solid-state method synthesis of SnO₂-decorated g-C₃N₄ nanocomposites with enhanced gas-sensing property to ethanol, *Materials* 10 (2017) 604, <https://doi.org/10.3390/ma10060604>.
- [45] D. Van Le, M.B. Nguyen, P.T. Dang, T. Lee, T.D. Nguyen, Synthesis of a UiO-66/g-C₃N₄ composite using terephthalic acid obtained from waste plastic for the photocatalytic degradation of the chemical warfare agent simulant, methyl paraoxon, *RSC Adv.* 12 (2022) 22367–22376, <https://doi.org/10.1039/d2ra03483b>.
- [46] X. Rao, H. Dou, D. Long, Y. Zhang, Ag₃PO₄/g-C₃N₄ nanocomposites for photocatalytic degrading gas phase formaldehyde at continuous flow under 420 nm LED irradiation, *Chemosphere* 244 (2020), <https://doi.org/10.1016/j.chemosphere.2019.125462>.
- [47] N.A. Chopan, A.H. Bhat, H.T.N. Chishti, Fabrication of polypyrrole-sensitized Ag₃PO₄/g-C₃N₄ Z-scheme heterojunction for photocatalytic and antibacterial activity, *New J. Chem.* 47 (2023) 15922–15941, <https://doi.org/10.1039/d3nj02774k>.
- [48] M.D. Donohue, G.L. Aranovich, Classification of Gibbs adsorption isotherms, *Adv. Colloid Interface Sci.* 76–77 (1998) 137–152, [https://doi.org/10.1016/S0001-8686\(98\)00044-X](https://doi.org/10.1016/S0001-8686(98)00044-X).
- [49] A.M. Varghese, K.S.K. Reddy, G.N. Karanikolos, An in-situ-grown Cu-BTC metal-organic framework/graphene oxide hybrid adsorbent for selective hydrogen

- storage at ambient temperature, Ind. Eng. Chem. Res. (2021), <https://doi.org/10.1021/acs.iecr.1c04710>.
- [50] M. Rahmani, A. Abbasi, M.S. Hosseini, Enhancing the visible light absorption of MOF-808 by surface decoration with sulfur and nitrogen co-doped carbon quantum dots: highly efficient photocatalyst for improved photocatalytic water remediation, Appl. Surf. Sci. 648 (2024) 159014, <https://doi.org/10.1016/j.apsusc.2023.159014>.
- [51] H. Ren, L. Ge, Q. Guo, L. Li, G. Hu, J. Li, The enhancement of photocatalytic performance of SrTiO₃ nanoparticles: via combining with carbon quantum dots, RSC Adv. 8 (2018) 20157–20165, <https://doi.org/10.1039/c8ra02103a>.
- [52] K. Chen, H. Feng, L. Li, M. Luo, S. Xue, J. Sang, Synthesis of dual Z-scheme flower-like spherical Ag₃PO₄/MoS₂/g-C₃N₄ photocatalyst with high photocatalytic performance, J. Mater. Sci. Mater. Electron. 33 (2022) 16077–16098, <https://doi.org/10.1007/s10854-022-08500-6>.
- [53] J. Xu, Y. Lu, F. Tao, P. Liang, P. Zhang, ZnO nanoparticles modified by carbon quantum dots for the photocatalytic removal of synthetic pigment pollutants, ACS Omega 8 (2023) 7845–7857, <https://doi.org/10.1021/acsomega.2c07591>.
- [54] X. Jiang, L. Wang, F. Yu, Y. Nie, Photodegradation of organic pollutants coupled with simultaneous photocatalytic evolution of hydrogen using quantum dot modified g-C₃N₄ catalysts under visible light irradiation photodegradation of organic pollutants coupled with simultaneous photocatalyst, ACS Sustain. Chem. Eng. 6 (10) (2018) 12695–12705, <https://doi.org/10.1021/acssuschemeng.8b01695>.
- [55] X. Jian, X. Liu, H. Yang, J. Li, X. Song, H. Dai, Z. Liang, Construction of carbon quantum dots/proton-functionalized graphitic carbon nitride nanocomposite via electrostatic self-assembly strategy and its application, Appl. Surf. Sci. 370 (2016) 514–521, <https://doi.org/10.1016/j.apsusc.2016.02.119>.
- [56] M. Hu, P. Zhu, M. Liu, J. Xu, M. Duan, J. Lin, Construction of Ag₃PO₄/TiO₂/C with p-n heterojunction using Shiff base-Ti complex as precursor: Preparation, performance and mechanism, Powder Technol. 393 (2021) 597–609, <https://doi.org/10.1016/j.powtec.2021.08.011>.
- [57] S. Hu, X. Chen, Q. Li, F. Li, Z. Fan, H. Wang, Y. Wang, B. Zheng, G. Wu, Fe³⁺ doping promoted N₂ photofixation ability of honeycombed graphitic carbon nitride: the experimental and density functional theory simulation analysis, Appl. Catal. B 201 (2017) 58–69, <https://doi.org/10.1016/j.apcatb.2016.08.002>.
- [58] S. Hu, X. Qu, P. Li, F. Wang, Q. Li, L. Song, Y. Zhao, X. Kang, Photocatalytic oxygen reduction to hydrogen peroxide over copper doped graphitic carbon nitride hollow microsphere: the effect of Cu(I)-N active sites, Chem. Eng. J. 334 (2018) 410–418, <https://doi.org/10.1016/j.cej.2017.10.016>.
- [59] S. Hu, X. Qu, J. Bai, P. Li, Q. Li, F. Wang, L. Song, Effect of Cu(I)-N active sites on the N₂ photofixation ability over flowerlike copper-doped g-C₃N₄ prepared via a novel molten salt-assisted microwave process: the experimental and density functional theory simulation analysis, ACS Sustain. Chem. Eng. 5 (2017) 6863–6872, <https://doi.org/10.1021/acssuschemeng.7b01089>.
- [60] B. Kumar, F.G. Tseng, Synergistic enhancement of seawater hydrogen generation via sulfur vacancy enriched and phases engineered CQD loaded CdS photocatalyst, Mater. Adv. 5 (2024) 1284–1300, <https://doi.org/10.1039/d3ma00741c>.
- [61] T. Qiang, S. Wang, L. Ren, X. Gao, Novel 3D Cu₂O/N-CQD/ZIF-8 composite photocatalyst with Z-scheme heterojunction for the efficient photocatalytic reduction of Cr (VI), J. Environ. Chem. Eng. 10 (2022) 108784, <https://doi.org/10.1016/j.jece.2022.108784>.
- [62] X. Dong, S. Zhang, H. Wu, Z. Kang, L. Wang, Facile one-pot synthesis of Mg-doped g-C₃N₄ for photocatalytic reduction of CO₂, RSC Adv. 9 (2019) 28894–28901, <https://doi.org/10.1039/c9ra04606b>.
- [63] X. Zhang, Y. Sui, F. Wei, J. Qi, Q. Meng, Y. Ren, Y. He, Self-supported 3D layered zinc/nickel metal-organic-framework with enhanced performance for supercapacitors, J. Mater. Sci. Mater. Electron. 30 (2019) 18101–18110, <https://doi.org/10.1007/s10854-019-02163-6>.
- [64] R. Ye, H. Fang, Y.Z. Zheng, N. Li, Y. Wang, X. Tao, Fabrication of CoTiO₃/g-C₃N₄ hybrid photocatalysts with enhanced H₂ evolution: Z-scheme photocatalytic mechanism insight, ACS Appl. Mater. Interfaces 8 (2016) 13879–13889, <https://doi.org/10.1021/acsami.6b01850>.
- [65] C.C. Wang, X.H. Yi, P. Wang, Powerful combination of MOFs and C₃N₄ for enhanced photocatalytic performance, Appl. Catal. B 247 (2019) 24–48, <https://doi.org/10.1016/j.apcatb.2019.01.091>.
- [66] Z. Zhang, Y. Chen, Z. Wang, C. Hu, D. Ma, W. Chen, T. Ao, Effective and structure-controlled adsorption of tetracycline hydrochloride from aqueous solution by using Fe-based metal-organic frameworks, Appl. Surf. Sci. 542 (2021) 148662, <https://doi.org/10.1016/j.apsusc.2020.148662>.
- [67] X. Hua, H. Chen, C. Rong, F. Addison, D. Dong, J. Qu, D. Liang, Z. Guo, N. Zheng, H. Liu, Visible-light-driven photocatalytic degradation of tetracycline hydrochloride by Z-scheme Ag₃PO₄/1T@2H-MoS₂ heterojunction: degradation mechanism, toxicity assessment, and potential applications, J. Hazard. Mater. 448 (2023) 130951, <https://doi.org/10.1016/j.jhazmat.2023.130951>.
- [68] M. Abdollahi, A. Larimi, Z. Jiang, F. Khorasheh, C. Ghotbi, Photocatalytic oxidative desulfurization of model fuel over visible light-active Cu-impregnated carbon-doped TiO₂, J. Clean. Prod. 380 (2022) 134968, <https://doi.org/10.1016/j.jclepro.2022.134968>.
- [69] P. Ghasemipour, M. Fattahi, B. Rasekh, F. Yazdian, Developing the ternary ZnO doped MoS₂ nanostructures grafted on CNT and reduced graphene oxide (RGO) for photocatalytic degradation of aniline, Sci. Rep. 10 (2020) 1–16, <https://doi.org/10.1038/s41598-020-61367-7>.
- [70] Y. Tian, M. Zhou, Y. Pan, X. Du, Q. Wang, MoS₂ as highly efficient co-catalyst enhancing the performance of Fe⁰ based electro-Fenton process in degradation of sulfamethazine: approach and mechanism, Chem. Eng. J. 403 (2021), <https://doi.org/10.1016/j.cej.2020.126361>.
- [71] D. Wang, S. Li, Q. Feng, Supramolecular self-assembled carbon nitride for the degradation of tetracycline hydrochloride, J. Mater. Sci. Mater. Electron. 29 (2018) 9380–9386, <https://doi.org/10.1007/s10854-018-8970-y>.
- [72] P. Punamiya, D. Sarkar, S. Rakshit, R. Datta, Effectiveness of aluminum-based drinking water treatment residuals as a novel sorbent to remove tetracyclines from aqueous medium, J. Environ. Qual. 42 (2013) 1449–1459, <https://doi.org/10.2134/jeq2013.03.0082>.
- [73] B. Gao, P.S. Yap, T.M. Lim, T.T. Lim, Adsorption-photocatalytic degradation of Acid Red 88 by supported TiO₂: effect of activated carbon support and aqueous anions, Chem. Eng. J. 171 (2011) 1098–1107, <https://doi.org/10.1016/j.cej.2011.05.006>.
- [74] N. Trung Dung, N. Hoang Duc, V. Thai Binh, V. Dinh Thao, M.B. Nguyen, L. Viet Ngan, N. Nhat Huy, A comprehensive study on the treatment of various organic pollutants by NiCoFe layered double oxide: material synthesis and characterization, decomposition mechanism exploration, and real water applications, Sep. Purif. Technol. 285 (2021) 120358, <https://doi.org/10.1016/j.seppur.2021.120358>.
- [75] W. Wu, Y. Sun, H. Zhou, In-situ construction of β-Bi₂O₃/Ag₂O photocatalyst from deactivated AgBiO₃ for tetracycline degradation under visible light, Chem. Eng. J. 432 (2022), <https://doi.org/10.1016/j.cej.2021.134316>.
- [76] R. Cestaro, L. Philippe, A. Serrà, E. Gómez, P. Schmutz, Electrodeposited manganese oxides as efficient photocatalyst for the degradation of tetracycline antibiotics pollutant, Chem. Eng. J. 462 (2023), <https://doi.org/10.1016/j.cej.2023.142202>.
- [77] C. Ding, Q. Zhu, B. Yang, E. Petropoulos, L. Xue, Y. Feng, S. He, L. Yang, Efficient photocatalysis of tetracycline hydrochloride (TC-HCl) from pharmaceutical wastewater using AgCl/ZnO/g-C₃N₄ composite under visible light: process and mechanisms, J. Environ. Sci. (China) 126 (2023) 249–262, <https://doi.org/10.1016/j.ies.2022.02.032>.
- [78] M. Balouiri, M. Sadiki, S.K. Ibsouda, Methods for in vitro evaluating antimicrobial activity: a review, J. Pharm. Anal. 6 (2016) 71–79, <https://doi.org/10.1016/j.jpha.2015.11.005>.
- [79] A. Khan, H. Wang, Y. Liu, A. Jawad, J. Ifthikar, Z. Liao, T. Wang, Z. Chen, Highly efficient α-Mn₂O₃–MnO₂-500 nanocomposite for peroxyomonosulfate activation: comprehensive investigation of manganese oxides, J. Mater. Chem. A 6 (2018) 1590–1600, <https://doi.org/10.1039/c7ta07942g>.